Cell Reports

Article

High-throughput functional analysis of autism genes in zebrafish identifies convergence in dopaminergic and neuroimmune pathways

Graphical abstract

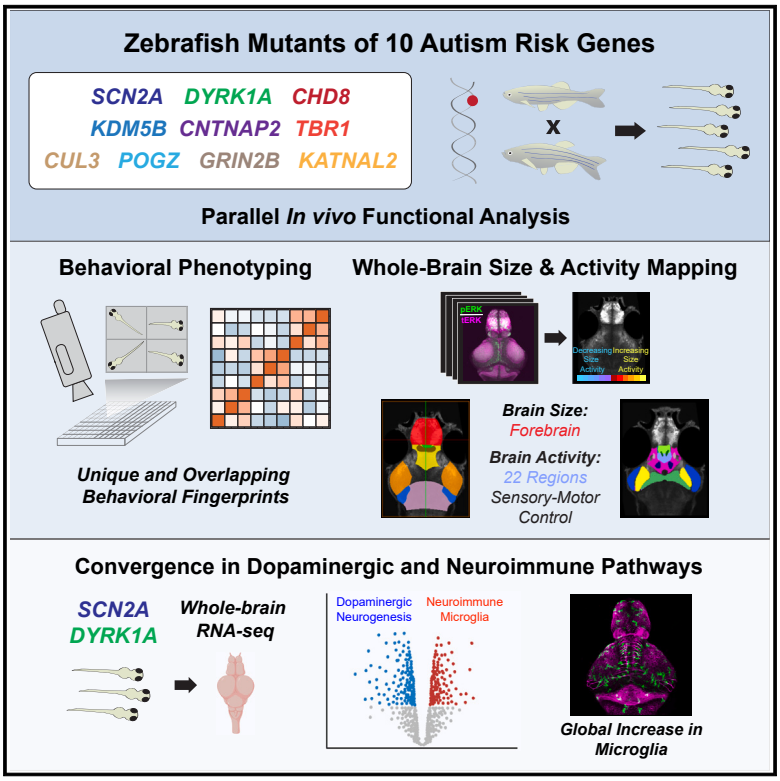

Highlights

- High-throughput behavioral phenotyping of 10 zebrafish ASD gene mutants
- The forebrain contributes the most to brain size differences across ASD genes
- Brain activity phenotypes converge on regions involved in sensory-motor control
- Convergence in dopaminergic and neuroimmune pathways for two ASD genes

Authors

Hellen Weinschutz Mendes, Uma Neelakantan, Yunqing Liu, ..., Xenophon Papademetris, Zuoheng Wang, Ellen J. Hoffman

Correspondence

ellen.hoffman@yale.edu

In brief

By analyzing the function of 10 autism genes in zebrafish, Weinschutz Mendes et al. identify distinct and overlapping phenotypes at the behavioral, brain structural, and circuit levels. They identify dopaminergic and microglial abnormalities as a point of convergence for two genes, and implicate neuroimmune dysfunction as relevant to autism biology.

Weinschutz Mendes et al., 2023, Cell Reports *42*, 112243
March 28, 2023
https://doi.org/10.1016/j.celrep.2023.112243

CellPress

Cell Reports

CellPress
OPEN ACCESS

Article

High-throughput functional analysis of autism genes in zebrafish identifies convergence in dopaminergic and neuroimmune pathways

Hellen Weinschutz Mendes,[1] Uma Neelakantan,[1] Yunqing Liu,[2] Sarah E. Fitzpatrick,[1,3,4,5] Tianying Chen,[1] Weimiao Wu,[2] April Pruitt,[1,3,4] David S. Jin,[1,3,4,6] Priyanka Jamadagni,[1] Marina Carlson,[1,3,4] Cheryl M. Lacadie,[7] Kristen D. Enriquez,[1] Ningshan Li,[2,8] Dejian Zhao,[9] Sundas Ijaz,[1] Catalina Sakai,[1] Christina Szi,[1] Brendan Rooney,[1] Marcus Ghosh,[10] Ijeoma Nwabudike,[1,4,5,11] Andrea Gorodezky,[1] Sumedha Chowdhury,[1] Meeraal Zaheer,[1] Sarah McLaughlin,[1] Joseph M. Fernandez,[1] Jia Wu,[1] Jeffrey A. Eilbott,[1] Brent Vander Wyk,[12] Jason Rihel,[10] Xenophon Papademetris,[7,13] Zuoheng Wang,[2] and Ellen J. Hoffman[1,3,14,*]

[1]Child Study Center, Yale School of Medicine, New Haven, CT 06510, USA
[2]Department of Biostatistics, Yale School of Public Health, New Haven, CT 06510, USA
[3]Department of Neuroscience, Yale School of Medicine, New Haven, CT 06510, USA
[4]Interdepartmental Neuroscience Program, Yale University, New Haven, CT 06510, USA
[5]MD-PhD Program, Yale School of Medicine, New Haven, CT 06510, USA
[6]Department of Neurology, Yale School of Medicine, New Haven, CT 06510, USA
[7]Department of Radiology and Biomedical Imaging, Yale School of Medicine, New Haven, CT 06510, USA
[8]SJTU-Yale Joint Center for Biostatistics and Data Science, Department of Bioinformatics and Biostatistics, School of Life Sciences and Biotechnology, Shanghai Jiao Tong University, Shanghai 200240, China
[9]Department of Genetics, Yale Center for Genome Analysis, Yale School of Medicine, New Haven, CT 06510, USA
[10]Department of Cell and Developmental Biology, University College London, Gower Street, London WC1E 6BT, UK
[11]Department of Psychiatry, Yale School of Medicine, New Haven, CT 06510, USA
[12]Department of Internal Medicine, Section of Geriatrics, Yale School of Medicine, New Haven, CT 06510, USA
[13]Department of Biomedical Engineering, Yale University, New Haven, CT 06510, USA
[14]Lead contact
*Correspondence: ellen.hoffman@yale.edu
https://doi.org/10.1016/j.celrep.2023.112243

SUMMARY

Advancing from gene discovery in autism spectrum disorders (ASDs) to the identification of biologically relevant mechanisms remains a central challenge. Here, we perform parallel *in vivo* functional analysis of 10 ASD genes at the behavioral, structural, and circuit levels in zebrafish mutants, revealing both unique and overlapping effects of gene loss of function. Whole-brain mapping identifies the forebrain and cerebellum as the most significant contributors to brain size differences, while regions involved in sensory-motor control, particularly dopaminergic regions, are associated with altered baseline brain activity. Finally, we show a global increase in microglia resulting from ASD gene loss of function in select mutants, implicating neuroimmune dysfunction as a key pathway relevant to ASD biology.

INTRODUCTION

There has been remarkable progress in recent years in our ability to identify genes that are strongly associated with autism spectrum disorders (ASDs), leading to the identification of >100 risk genes.[1–5] These genes of large effect were identified by the presence of recurrent, *de novo* damaging mutations in affected individuals by whole-exome sequencing and are likely to shed light on relevant pathophysiological mechanisms. While these genes represent seemingly disparate molecular functions, common biological pathways are beginning to emerge, such as gene expression regulation and neuronal communication.[1,4,5] However, ASD genes are highly pleiotropic, further complicating efforts to identify unifying pathophysiology.[6] To address this, studies have focused on identifying convergent mechanisms across genes, with the rationale that elucidating shared pathways might reveal molecular targets with therapeutic potential.[7]

Recent studies have found evidence for biological convergence across risk genes. Co-expression network and integrative genomics analyses identified strong enrichment of ASD gene expression in excitatory and inhibitory neurons during the mid to late fetal period,[1,8,9] providing evidence for excitatory-inhibitory (E/I) imbalance in the developing brain as a central pathway underlying ASDs.[10] *In vitro* studies provide additional support for this mechanism, showing that disruption of three ASD genes in human cortical organoids results in asynchronous development of excitatory and inhibitory neuron populations.[11] In addition, studies have implicated altered neural proliferation and differentiation resulting from ASD gene loss of function.[12] *In vivo* studies

in *Xenopus* demonstrated a critical role of 10 ASD genes in neurogenesis,[13] while targeting 35 ASD- and neurodevelopmental disorder-associated genes in the mouse cortex revealed a key function of these genes in both the neuronal and glial lineages,[14] highlighting a role for neurogenesis and gliogenesis in ASD biology.

At the same time, there is growing recognition that ASD genes have unique neurodevelopmental effects, which may be equally important for defining biologically relevant sub-groups and developing targeted treatments. For example, a functional magnetic resonance imaging analysis of 16 mouse mutants with ASD-associated mutations identified brain connectivity sub-types among mutants despite the presence of divergent phenotypes.[15] Similarly, while mouse mutants of 26 ASD genes displayed heterogeneous neuroanatomical phenotypes, clustering these mutants by shared features led to the identification of gene sub-groups.[16] Therefore, categorizing genes based on shared biology despite their heterogeneity might represent a path toward precision medicine in ASDs, bridging the gap between gene discovery and actionable biological mechanisms.

In this study, we sought to leverage the unique features of zebrafish to define the neurodevelopmental effects of 10 ASD genes, with the goal of identifying functionally meaningful phenotypes across risk genes. Zebrafish offer important advantages in this regard, including direct visualization of the developing vertebrate brain in transparent embryos, amenability to large-scale behavior-based screens, and ease of genetic manipulation.[17–20] Our group and others have already demonstrated the strengths of this system for pharmaco-behavioral and genetic screens relevant to ASDs and other neuropsychiatric disorders.[21,22] There is also compelling evidence for the conservation of neural mechanisms in zebrafish and mammals at the level of gene expression, neurotransmitter systems, pharmacological pathways, and basic neural circuits,[23–29] highlighting the translational potential of zebrafish for elucidating biological mechanisms relevant to ASDs.

Here, we establish a pipeline for the *in vivo* functional analysis of ASD genes in zebrafish. We identify unique and shared phenotypes in zebrafish mutants of 10 ASD genes at multiple levels by incorporating high-throughput, automated behavioral assays, whole-brain structural and circuit analyses, and RNA sequencing (RNA-seq). While no two mutants share identical phenotypes across modalities, we find clear evidence that ASD gene dosage impacts basic arousal and sensory processing behaviors, brain size, and activity in the developing vertebrate brain. Our analysis demonstrates that ASD genes broadly impact brain size and identifies the forebrain (telencephalon) as the most significant contributor to size phenotypes. Whole-brain activity mapping reveals significant differences in baseline activity in the thalamus and posterior tuberculum, and identifies dopaminergic regions involved in sensory-motor control as a point of convergence. Finally, by performing RNA-seq in two ASD gene mutants with the most robust phenotypes, *DYRK1A* and *SCN1A/SCN2A*, we find striking evidence for the conservation of molecular pathways downstream of ASD genes in zebrafish and mammals and uncover evidence for dopaminergic and neuroimmune dysfunction in the developing brain relevant to ASD biology.

RESULTS

Generation of zebrafish ASD gene mutants

We selected 10 genes that are strongly associated with ASDs for functional analysis in zebrafish (Figure 1A). In addition to the syndromic ASD gene, *CNTNAP2*, which we previously studied,[21] we targeted another nine genes ascertained by whole-exome sequencing,[1,3–5] which were selected based on evidence for biological convergence by co-expression network analyses in humans.[8] These genes span a range of biological functions and represent pathways implicated in ASDs, including gene expression regulation (*CHD8*, *CUL3*, *KDM5B*, *POGZ*, and *TBR1*), neuronal communication (*CNTNAP2*, *SCN1A/SCN2A*, and *GRIN2B*), and the cytoskeleton (*DYRK1A* and *KATNAL2*).[1] All 10 genes have an SFARI gene score of 1 (false discovery rate <0.1) or are syndromic ASD-associated genes,[32] indicating that they are strongly associated with ASD risk.

To analyze the effect of gene loss of function (LoF) in the developing brain, we targeted the zebrafish ortholog(s) of each ASD gene using CRISPR-Cas9, TALENs, or zinc finger nucleases and generated two stable mutant lines for each gene carrying early frameshift mutations that are predicted to cause a truncation (Figures 1A and S1A–S1I, Table S1, STAR Methods). For genes that are duplicated in zebrafish, both paralogs were targeted. Zebrafish orthologs show a high degree of conservation with human genes, displaying on average approximately 70% identity at the amino acid level (Table S1). Most homozygous and all heterozygous mutants lack gross morphological phenotypes and survive to adulthood with the exception of homozygous *cul3* and *scn1lab* mutants, which display gross morphological phenotypes as larvae (Figures S1J–S1K). Phenotyping analyses were performed in homozygous and heterozygous mutants for all genes except *cul3*, where intermediate genotypes (e.g., *cul3a*$^{\Delta 7/\Delta 7}$*cul3b*$^{\Delta 20/+}$) were used because of severe morphological abnormalities in homozygotes.

Developmental trajectory of ASD gene expression in zebrafish

To characterize ASD gene expression in the developing zebrafish brain, we performed whole mount *in situ* hybridization. We found that the orthologs of ASD genes are broadly expressed in the zebrafish CNS at 24 to 48 h post-fertilization, with many genes showing strong expression in the telencephalon and midbrain-hindbrain boundary (Figure 1B), which are neurogenic zones.[33] To investigate how ASD gene expression in zebrafish compares with the human brain, we mapped zebrafish transcriptomic datasets from embryonic and larval stages[30] onto the human BrainSpan developmental transcriptome[31] using principal component analysis.[13] Our analysis reveals that zebrafish development follows a clear chronological trajectory that can be mapped onto related stages of human brain development (Figures 1C and S1L). Interestingly, we show that embryonic stages when ASD genes are expressed in the zebrafish CNS (Figure 1B) correspond most closely with the human mid-prenatal period, consistent with their expression patterns in the human brain,[8,9] while the larval stages when our phenotyping assays are performed (5–6 days post-fertilization [dpf]) map to the late pre-natal stage in humans (Figure 1C). Therefore, the time points that we study in zebrafish

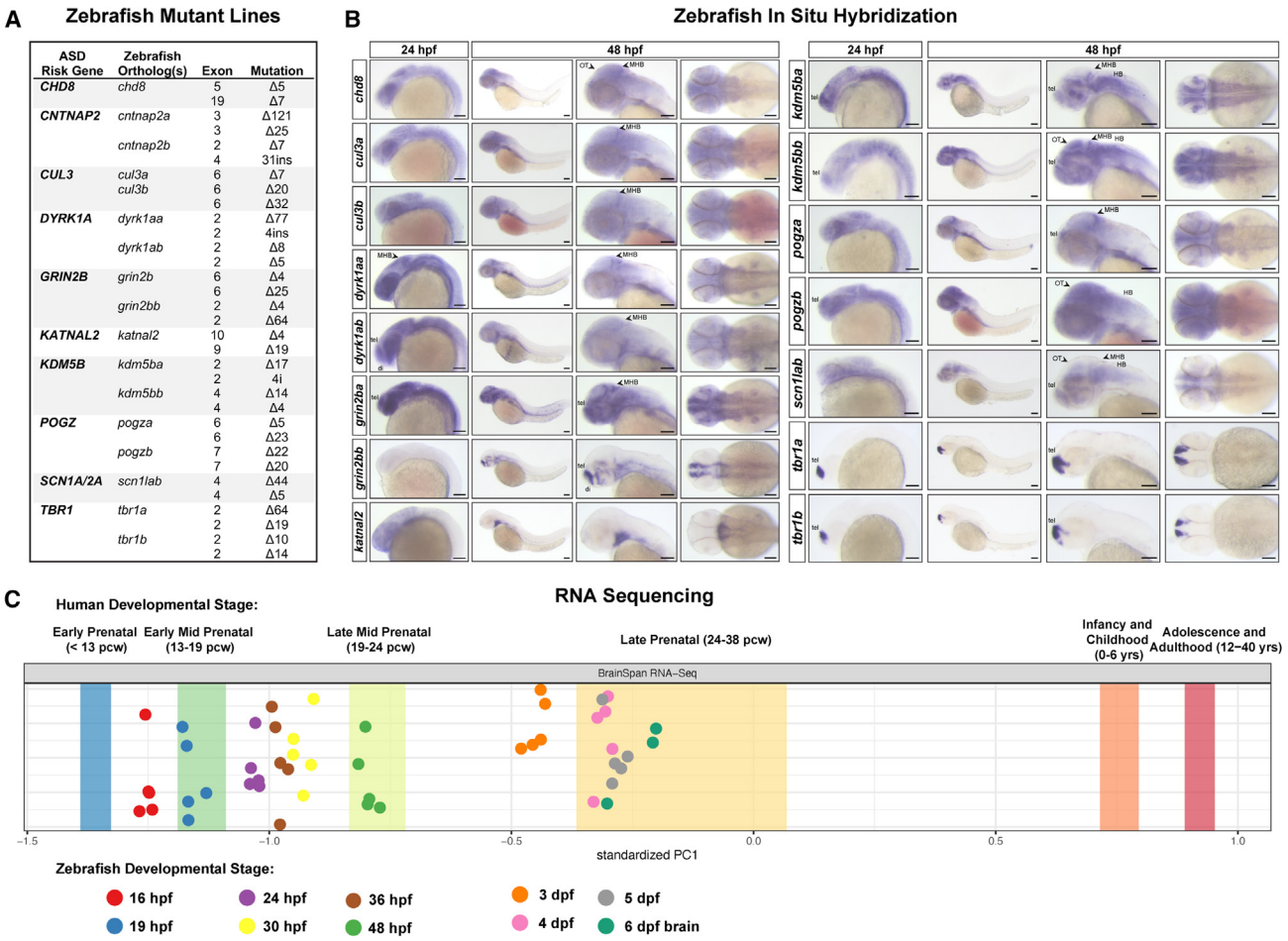

ASD Risk Gene	Zebrafish Ortholog(s)	Exon	Mutation
CHD8	*chd8*	5	Δ5
		19	Δ7
CNTNAP2	*cntnap2a*	3	Δ121
		3	Δ25
	cntnap2b	2	Δ7
		4	31ins
CUL3	*cul3a*	6	Δ7
	cul3b	6	Δ20
		6	Δ32
DYRK1A	*dyrk1aa*	2	Δ77
		2	4ins
	dyrk1ab	2	Δ8
		2	Δ5
GRIN2B	*grin2b*	6	Δ4
		6	Δ25
	grin2bb	2	Δ4
		2	Δ64
KATNAL2	*katnal2*	10	Δ4
		9	Δ19
KDM5B	*kdm5ba*	2	Δ17
		2	4i
	kdm5bb	4	Δ14
		4	Δ4
POGZ	*pogza*	6	Δ5
		6	Δ23
	pogzb	7	Δ22
		7	Δ20
SCN1A/2A	*scn1lab*	4	Δ44
		4	Δ5
TBR1	*tbr1a*	2	Δ64
		2	Δ19
	tbr1b	2	Δ10
		2	Δ14

Figure 1. ASD gene expression in zebrafish and mutant generation

(A) Zebrafish mutant lines. See Table S1 and Figures S1A–S1I for mutant sequences.

(B) Whole-mount RNA *in situ* hybridization of ASD gene orthologs in zebrafish at 24 and 48 hpf. For *cntnap2a* and *cntnap2b*, see Hoffman et al. (2016).[21] Lateral views are shown in the left three panels; dorsal views are shown in the right panel. Anterior to the left; tel, telencephalon; di, diencephalon; MHB, midbrain-hindbrain boundary; OT, optic tectum; HB, hindbrain. Scale bars, 0.1 mm.

(C) Mapping zebrafish RNA-seq datasets[30] to the human BrainSpan developmental transcriptome RNA-seq dataset[31] using principal component analysis.[13] Principal component 1 (PC1) is plotted. Bands represent the 95% confidence interval of the mean PC1 value for human developmental stages. Biological replicates of zebrafish samples are shown as points. pcw, postconception weeks; hpf, hours post-fertilization; dpf, days post-fertilization. See Figure S1L for the full PCA.

are likely to be highly relevant for understanding ASD gene function at related stages of human brain development.

Convergence and divergence define basic behavioral phenotypes

We first aimed to establish that ASD gene LoF affects basic arousal and sensory processing behaviors in zebrafish to obtain a readout of circuit-level effects resulting from gene disruption. We performed quantitative behavioral profiling using high-throughput, automated assays of sleep-wake activity[24,29] and visual-startle responses[34] (Figures 2A and 2B, STAR Methods) and measured 24 sleep-wake and startle parameters in all 20 mutant lines (Table S2). In total, we tested >7,500 background-matched larvae from heterozygous incrosses at 6 dpf using two mutant lines per gene (Figure 1A). We defined unique behavioral fingerprints for each ASD gene mutant (Figure 2C), which reveal differential effects of ASD gene LoF on the circuitry underlying these behaviors. Using hierarchical clustering, we found that the behavioral profiles of independent mutant lines of the same gene co-cluster (Figure 2C), indicating that mutations in each gene result in similar behavioral features.

We identified a spectrum of convergent and divergent behavioral phenotypes across mutants (Figure 2C). For example, mutants of *scn1lab* and *dyrk1a* display the most robust behavioral phenotypes, including increased responses to lights-on stimuli in *scn1lab* mutants and decreased responses to lights-off stimuli in *dyrk1a* mutants (Figures 2D and 2E). Both mutants show decreased daytime activity, while only *scn1lab* mutants exhibit night-time hyperactivity (Figures 2D and 2E). These behaviors likely reflect conserved roles of these genes, given the association

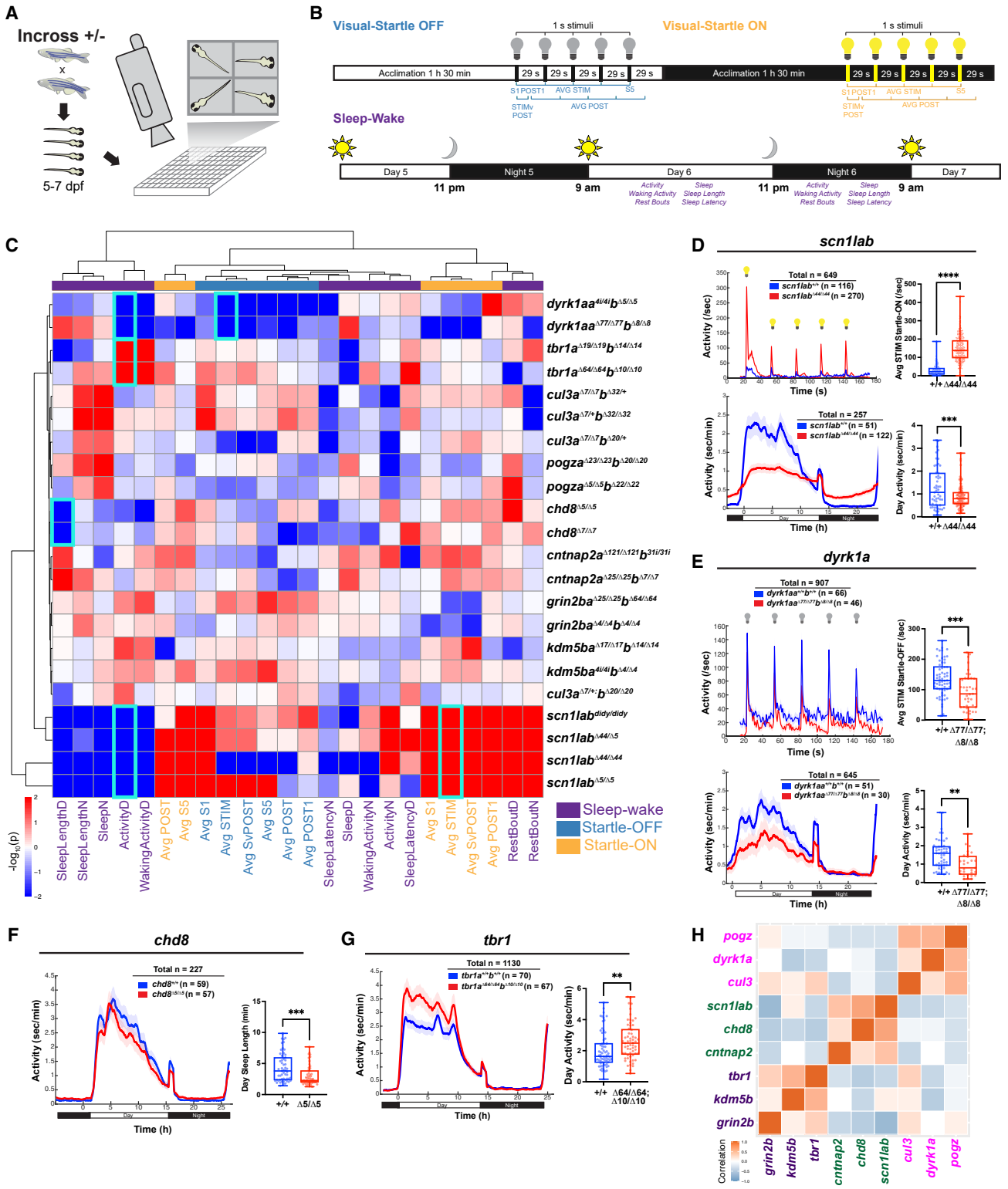

Figure 2. Behavioral phenotypes in zebrafish ASD gene mutants

(A and B) Experimental setup and behavioral assays. *Visual-startle*: Larvae are exposed to five 1-s flashes of lights-off or -on stimuli at 29-s intervals at 5 dpf. *Sleep-wake*: Larvae are exposed to a 14 h:10 h white light:dark schedule at 5–7 dpf. Visual-startle and sleep-wake parameters are shown (see STAR Methods).

(legend continued on next page)

of human mutations in *DYRK1A* with visual deficits[35] and *SCN1A* with increased sensitivity to visual stimuli[36]; both genes have been associated with sleep disturbance in humans.[37,38] *chd8* mutants display a highly specific phenotype of decreased daytime sleep length (Figure 2F), consistent with a conserved role of this gene in regulating sleep architecture in *Drosophila* and humans,[39] while *tbr1* mutants exhibit daytime hyperactivity (Figure 2G). Modestly increased locomotor activity was also observed in *Tbr1* mouse mutants carrying an ASD-associated *de novo* mutation.[40] Heterozygous mutants display intermediate phenotypes reflecting gene dosage effects (Figures S2A–S2J). Additional behavioral phenotypes, including night-time hyperactivity in *cntnap2* mutants,[21] are shown in Figures S2F–S2J.

Given the heterogeneity observed in mutant behaviors, we sought to identify gene sub-groups, which might represent shared circuit-level functions. To this end, we performed correlation analyses across mutants, prioritizing mutant lines with the most robust phenotypes for each gene. Our analysis identified three distinct sub-groups of ASD genes with highly correlated behavioral features (Figures 2H and S2K). Interestingly, the genes in these sub-groups have different biological functions (e.g., *chd8*, *scn1lab*, and *cntnap2*), yet related behavioral outcomes. This suggests that quantitative behavioral profiling can be leveraged to categorize ASD genes in functionally meaningful ways. Therefore, our analysis reveals both highly pleiotropic effects of ASD genes on basic behaviors and defines ASD gene clusters based on behavioral sub-types.

Brain size differences cluster in neurogenic regions

Given that altered brain growth has been described in ASDs,[41] we next investigated the effect of ASD gene LoF on brain size. We sought to determine the extent to which similar brain regions might be impacted across risk genes, representing shared vulnerabilities. To do this, we mapped confocal images of whole larval brains at 6 dpf immunostained for total extracellular signal-related kinase (tERK) onto a standard zebrafish reference brain[42] (Figure 3A, STAR Methods). Regional differences in brain volume were quantified in 8 major brain regions[22,42] (Figure 3B) in >600 background-matched homozygous, heterozygous, and wild-type fish from a total of 10 mutant lines. Our analysis identified unique brain size phenotypes in most homozygous mutants affecting multiple regions (Figure 3C, Table S3). Homozygous *dyrk1a* mutants display the most robust phenotype of significantly reduced brain size in all regions with the most prominent effects in the forebrain ($p = 1 \times 10^{-10}$, linear mixed model) (Figures 3D–3F). Intermediate phenotypes are also present in *dyrk1a* heterozygotes indicating gene-dosage effects (Figures S3A–S3C). The decrease in brain size in homozygous larvae (approximately 20%) is not associated with an equivalent decrease in body length (approximately 5%) (Figure S3D), indicating a specific effect of *dyrk1a* LoF on brain size. This is consistent with a conserved role of *DYRK1A* in regulating brain size in *Drosophila*, *Xenopus*, and mammals.[13,43,44] Brain volume phenotypes were also observed in mutants of *scn1lab*, *chd8*, *tbr1*, *kdm5b*, and *cul3*, primarily affecting the forebrain (telencephalon) and midbrain-hindbrain boundary (Figures 3C and 3G), which are neurogenic regions where these genes are highly expressed (Figure 1B).

To characterize shared phenotypes, we identified the brain regions most strongly associated with size differences by calculating the combined p value for each region across homozygous mutants and $cul3a^{\Delta7/\Delta7}cul3b^{\Delta20/+}$ using Fisher's method. Initially *dyrk1a* was excluded from this analysis given the magnitude of its phenotype. This analysis showed that the forebrain (telencephalon) is the most significant contributor to brain size differences ($p = 8.32 \times 10^{-6}$, Fisher's combined probability test), followed by the cerebellum ($p = 1.35 \times 10^{-4}$) (Figures 3H and S3E). Both the forebrain and cerebellum also display the largest percent change in volume (−4.46% and −5.39%; 1.15×10^5 μm^3 and 9.74×10^4 μm^3, respectively). This is in line with our observation of size phenotypes affecting the forebrain and midbrain-hindbrain boundary (Figure 3G), suggesting a vulnerability of neurogenic regions to ASD gene LoF. The forebrain is the most significant contributor to brain size ($p = 4.9 \times 10^{-13}$) and volume differences (−6.36%, 1.64×10^5 μm^3) when *dyrk1a* is included in the analysis (Figure S3F). Overall, our findings implicate a role for ASD genes in regulating brain size in neurogenic regions, particularly the forebrain.

ASD gene mutants display heterogeneous brain activity phenotypes

We reasoned that because ASD gene mutants display behavioral and brain size phenotypes, they might also exhibit differences in baseline brain activity, reflecting common circuit-level effects of gene LoF. To investigate this, we performed whole-brain activity mapping in freely swimming larvae at 6 dpf by immunostaining brains for phosphorylated-ERK (pERK), which labels active neurons, and tERK.[42] Using a custom analysis pipeline, we conducted a voxel-by-voxel comparison of the pERK/tERK ratio as a readout of active neurons in >600 background-matched homozygous, heterozygous, and wild-type fish from 10 mutant lines (Figures 4A and S4A). Overall, we found that more mutants show significant differences in baseline activity

(C) Hierarchical clustering of mutant behavioral fingerprints. Each rectangle represents the signed -$\log_{10}$-transformed p values from linear mixed models (LMM) comparing mutant and background-matched wild-type fish (red, increased in mutant; blue, decreased in mutant). Behavioral parameters from startle-off (light blue), startle-on (orange), and sleep-wake (purple) are shown. All mutant lines are shown except *katnal2*, which lacks consistently significant behavioral features (Figure S2A). Three mutant lines and transheterozygotes ($scn1lab^{\Delta44/\Delta5}$) are shown for *scn1lab*. Behavioral features shown in individual graphs (D–G) are outlined in cyan. Mean and SD values for all groups and beta and p values for all behavioral parameters are shown in Table S2.

(D–G) Significant behavioral phenotypes in ASD gene mutants: increased responses to lights-on stimuli, daytime hypoactivity, and night-time hyperactivity in $scn1lab^{\Delta44/\Delta44}$ (D); decreased responses to lights-off stimuli and daytime hypoactivity in $dyrk1aa^{\Delta77/\Delta77}dyrk1ab^{\Delta8/\Delta8}$ (E); decreased daytime sleep bout length in $chd8^{\Delta5/\Delta5}$ (F); and daytime hyperactivity in $tbr1a^{\Delta64/\Delta64}tbr1b^{\Delta10/\Delta10}$ (G). Sleep-wake time series graphs in (D–G) show a rolling average of activity data points every 50 min. ****$p < 0.0001$, ***$p < 0.001$, **$p < 0.01$ (one-way ANOVA).

(H) Correlation analysis across all 24 behavioral parameters identifies three sub-groups with related phenotypes: (i) $scn1lab^{\Delta44/\Delta44}$, $chd8^{\Delta5/\Delta5}$, $cntnap2a^{\Delta121/\Delta121}cntnap2b^{31ins/31ins}$; (ii) $pogza^{\Delta23/\Delta23}pogzb^{\Delta20/\Delta20}$, $dyrk1aa^{\Delta77/\Delta77}dyrk1ab^{\Delta8/\Delta8}$, $cul3a^{\Delta7/+}cul3b^{\Delta32/\Delta32}$; and (iii) $tbr1a^{\Delta64/\Delta64}tbr1b^{\Delta10/\Delta10}$, $kdm5ba^{\Delta17/\Delta17}kdm5bb^{\Delta14/\Delta14}$, $grin2ba^{\Delta25/\Delta25}grin2bb^{\Delta64/\Delta64}$.

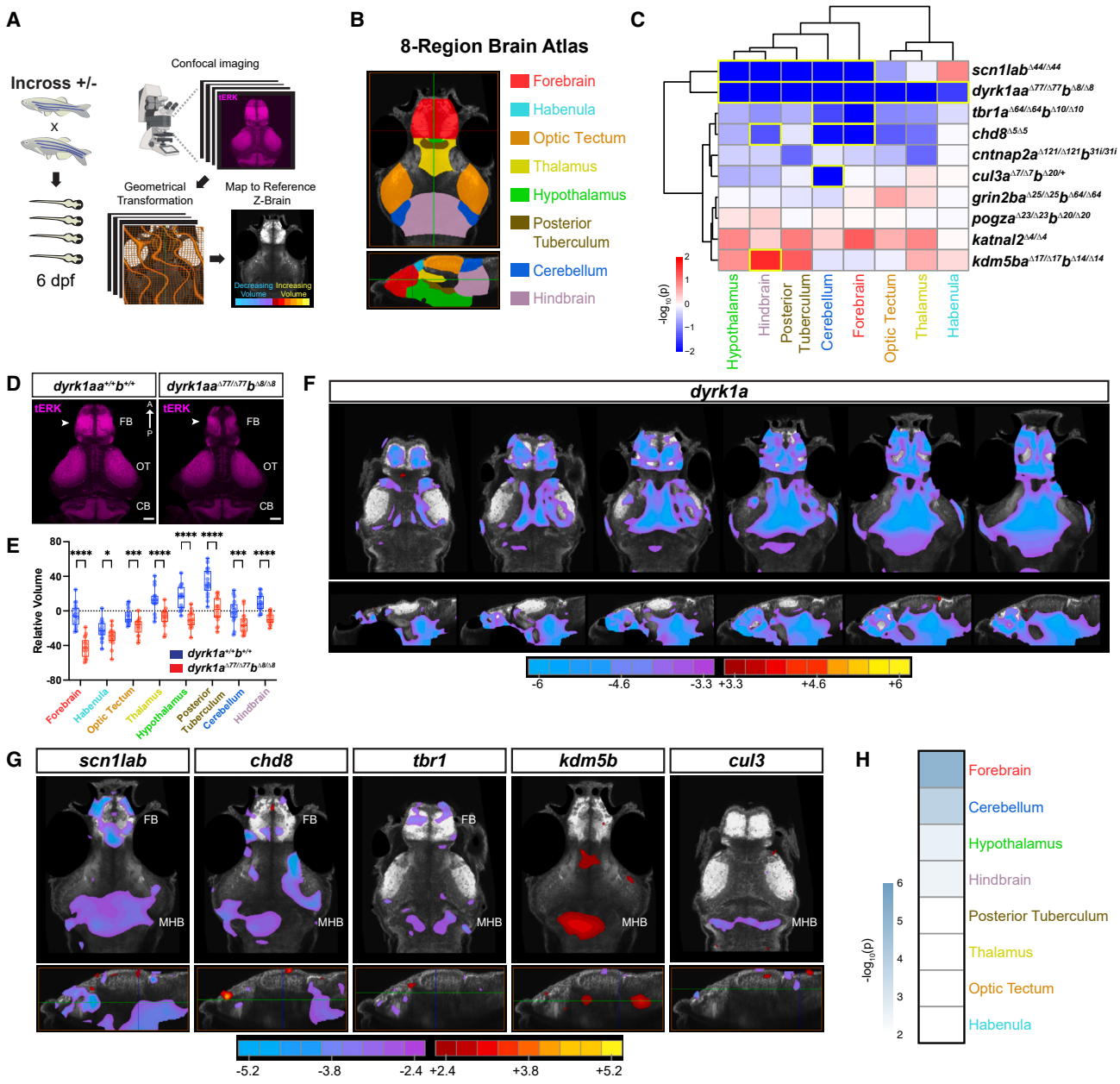

Figure 3. Zebrafish mutants of ASD genes display brain size phenotypes

(A) Whole-brain volume mapping pipeline (STAR Methods).

(B) Eight-region zebrafish brain atlas derived from Thyme et al. (2019) and Randlett et al. (2015).[22,42]

(C) Hierarchical clustering of regional brain volume measurements comparing mutant and background-matched wild-type fish. Each rectangle in the clustergram represents the signed -$\log_{10}$-transformed p values from linear mixed models (LMM) (red, increased in mutant; blue, decreased in mutant). Regions with significant volume differences by LMM ($p < 0.05$) are outlined in yellow. p-values for homozygous and heterozygous mutants are shown in Figure S3A. For raw volume quantifications by region for all fish, see Table S3.

(D) tERK-immunostained brains of *dyrk1aa*$^{\Delta 77/\Delta 77}$*dyrk1ab*$^{\Delta 8/\Delta 8}$ and wild-type larvae at 6 dpf. Note the decrease in forebrain volume in mutants (arrowheads). Dorsal views. FB, forebrain; OT, optic tectum; CB, cerebellum. Scale bar, 50 μm.

(E) Regional brain volume differences in *dyrk1aa*$^{\Delta 77/\Delta 77}$*dyrk1ab*$^{\Delta 8/\Delta 8}$ (n = 18) and wild-type (n = 18) relative to the standard zebrafish reference brain[42] (dotted line). ****$p < 0.0001$, ***$p < 0.001$, *$p < 0.05$ (one-way ANOVA).

(F) Voxel-wise *Z* score values representing brain volume differences in *dyrk1aa*$^{\Delta 77/\Delta 77}$*dyrk1ab*$^{\Delta 8/\Delta 8}$ versus background-matched wild-type larvae. Images shown from left to right represent sequential slices: axial views, top row, dorsal to ventral; sagittal views, bottom row, lateral to medial. Scale bar, *Z* score (red/yellow, increased in mutant; cyan/purple, decreased in mutant).

(G) Voxel-wise *Z* score values representing brain volume differences for the following lines: *scn1lab*$^{\Delta 44/\Delta 44}$, *chd8*$^{\Delta 5/\Delta 5}$, *tbr1a*$^{\Delta 64/\Delta 64}$*tbr1b*$^{\Delta 10/\Delta 10}$, *kdm5ba*$^{\Delta 17/\Delta 17}$*kdm5bb*$^{\Delta 14/\Delta 14}$, and *cul3a*$^{\Delta 7/\Delta 7}$*cul3b*$^{\Delta 20/+}$. Axial views, top row; sagittal views, bottom row. The horizontal green line in the sagittal view

(legend continued on next page)

(Figure 4B) compared with size (Figure 3C), and that activity phenotypes are generally more robust than volume phenotypes, suggesting that ASD gene LoF has a greater impact on brain activity versus size. In addition, the activity and volume measurements in the eight major brain regions (Figure 3B) are not highly correlated across mutants (Figure S4B), indicating these effects are independent of each other.

We identified unique brain activity phenotypes across ASD gene mutants (Figure 4B, Table S4). As in our analysis of mutant behavior, we found that ASD gene LoF results in a range of brain activity phenotypes, with no two mutants showing identical patterns of altered baseline activity. Homozygous *scn1lab* mutants display the strongest phenotype, characterized by significantly decreased activity throughout the brain, most prominently in the forebrain (telencephalon) and habenula (Figures 4C–4E). *scn1lab* heterozygotes show moderately decreased activity in these regions (Figures S4C and S4D), indicating gene dosage effects. Both *dyrk1a* and *chd8* mutants have significantly decreased baseline activity in several regions, including the thalamus and posterior tuberculum, while *cntnap2* mutants exhibit a striking increase in activity in multiple regions, including the thalamus and hypothalamus (Figure 4F). Heterozygotes exhibit intermediate phenotypes (Figures S4A, S4E and S4F). Additional significant phenotypes include increased activity in the thalamus in *kdm5b* mutants and decreased activity in the bilateral habenula in *tbr1* mutants (Figure 4F).

Despite the heterogeneity observed in brain activity, we reasoned that overlapping phenotypes might represent convergence at a circuit level. To identify shared regions that show differences in baseline activity across mutants, we calculated the combined p value from the eight major brain regions across homozygous mutants and $cul3a^{\Delta 7/\Delta 7}cul3b^{\Delta 20/+}$ using Fisher's method. *scn1lab* was excluded from this analysis because of the severity of its phenotype, which otherwise recapitulates the phenotype of the *scn1lab* mutant alone (Figures 4D and S4G). Our analysis of the remaining mutants identified the thalamus ($p = 9.55 \times 10^{-9}$, Fisher's combined probability test), followed by the posterior tuberculum ($p = 7.08 \times 10^{-7}$), as the most significant contributors to brain-wide activity differences (Figures 4G and S4H). This suggests that the thalamus is particularly vulnerable to alterations in baseline activity resulting from ASD gene LoF, unlike brain volume, where the forebrain (telencephalon) is most significantly affected by size differences (Figure 3H). Together, brain activity mapping in ASD gene mutants identifies a range of unique and shared phenotypes and implicates the thalamus as a main contributor to circuit-level differences.

Brain activity phenotypes converge on 22 neuroanatomical regions

To characterize brain activity phenotypes with greater specificity, we mapped whole-brain activity (pERK/tERK) datasets from homozygous and heterozygous mutants versus background-matched wild-type fish onto a zebrafish brain atlas containing 149 neuroanatomical regions and neural cell type clusters[42] (Figure 5A). We defined whole-brain activity fingerprints for each ASD gene mutant across the 149 regions and found that these fingerprints broadly cluster by major brain sub-division (telencephalon, diencephalon, mesencephalon, and rhombencephalon) (Figure S5A), reflecting similar activity patterns within these regions. Next, we asked which of the 149 regions shows significant differences in baseline activity in most mutants, representing convergence. To this end, we ranked regions based on their significance in the greatest number of mutants, as opposed to their relative strength in individual mutants. Our analysis identified 22 of the 149 regions with significant differences in at least five mutants ($p < 0.05$, linear mixed model) (Figures 5B and 5C, Table S5). Of the 22 regions, 16 (73%) are in the diencephalon and include regions that broadly function in sensory-motor control and sleep regulation, such as the dorsal and ventral thalamus, posterior tuberculum, pretectum, and pre-optic area (Figure 5C), highlighting a vulnerability of these regions to ASD gene LoF. In addition, 7 of the top 22 regions, including the dorsal thalamus, show significant differences in baseline activity in at least 6 mutants ($p < 0.05$, linear mixed model) (Figure 5C [asterisks], Figures S5B and S5C, Table S5). Baseline activity in these regions is significantly decreased in *scn1lab* and *dyrk1a* mutants (Figures 5D and 5E), which also display the most robust sensory responsiveness and sleep-wake phenotypes (Figures 2D and 2E). Furthermore, most heterozygous mutants display intermediate phenotypes (Figures S5D–S5I), providing strong evidence that ASD gene dosage affects baseline activity in these seven regions.

We next investigated the neural cell types present among the top 22 regions. Intriguingly, we found that 5 of the 22 regions are associated with dopaminergic neuron development, including the pre-tectal dopaminergic cluster, *otpb* and *vmat2* neuron clusters,[45,46] and the posterior tuberculum, which contains dopaminergic neurons that are functionally related to midbrain dopaminergic neurons in the mammalian ventral tegmental area (VTA)[47] (Figure 5C [italics]). In addition, two of the top seven regions with significant activity differences in six mutants are dopaminergic: the pre-tectal dopaminergic cluster and anterior pre-tectal cluster of *vmat2* neurons (Figures S5B and S5C). Therefore, our analysis demonstrates that ASD gene disruption affects baseline activity in 22 neuroanatomical regions broadly associated with sensory-motor regulation and provides evidence for convergence in dopaminergic regions.

Dysregulated pathways in *scn1lab* and *dyrk1a* mutants are highly conserved

To identify molecular mechanisms underlying brain size, activity, and behavioral phenotypes, we performed whole-brain RNA-seq

indicates the slice shown in the axial view. FB, forebrain; MHB, midbrain-hindbrain boundary. Scale bar, *Z* score (red/yellow, increased in mutant; cyan/purple, decreased in mutant). For the number of animals used in imaging experiments, see STAR Methods (average n = 23–26 per genotype in two to four independent clutches).

(H) Genotype-level p values for each brain region combined for all homozygous mutants and $cul3a^{\Delta 7/\Delta 7}cul3b^{\Delta 20/+}$, excluding *dyrk1a*, using Fisher's method. Scale represents the $-\log_{10}$-transformed combined p value. The forebrain (telencephalon) shows the most significant difference in volume ($p = 8.32 \times 10^{-6}$, Fisher's combined probability test).

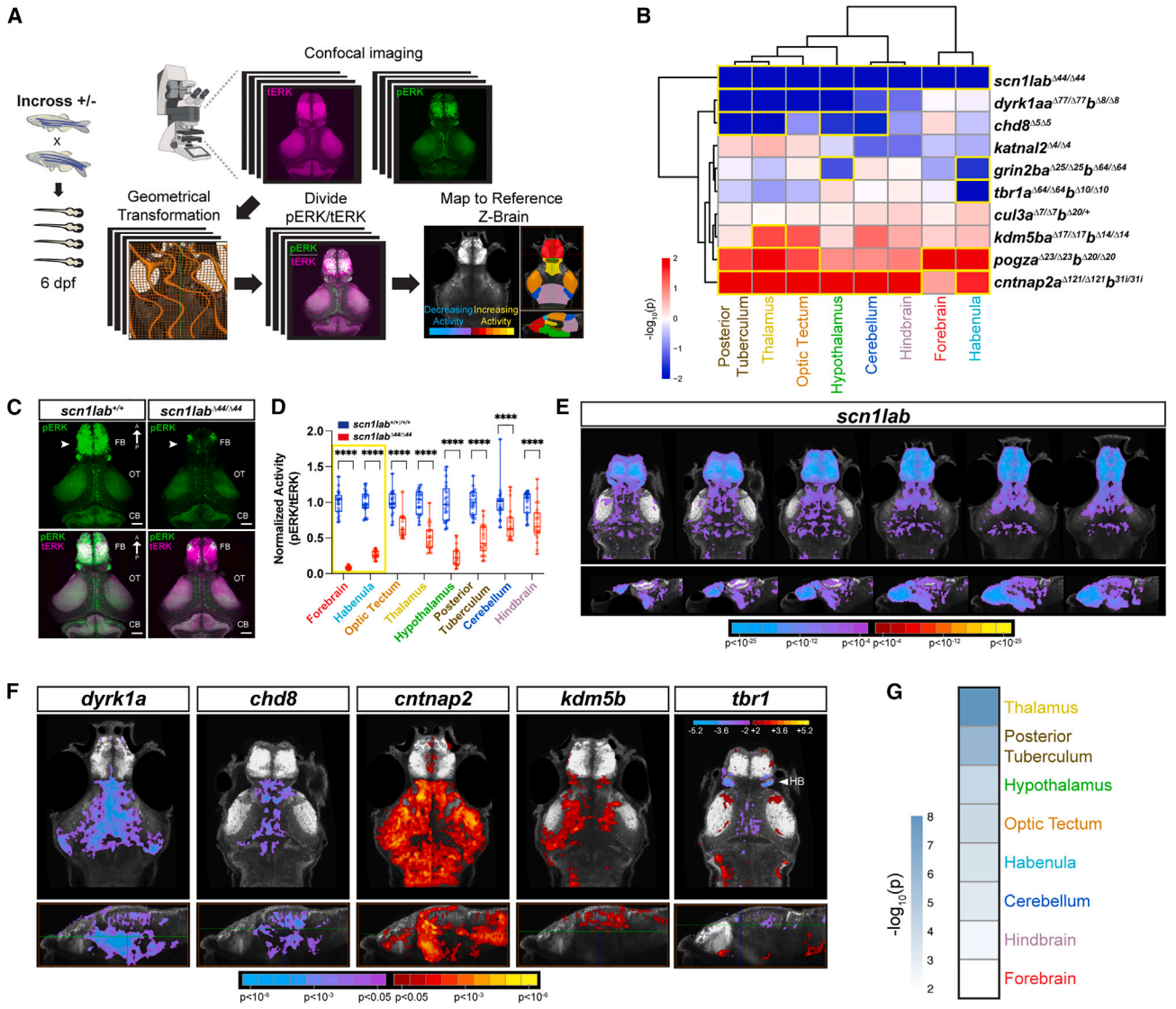

Figure 4. Altered baseline brain activity in zebrafish ASD gene mutants

(A) Whole-brain activity mapping pipeline (STAR Methods).

(B) Hierarchical clustering of regional brain activity (pERK/tERK) in mutant versus background-matched wild-type fish using linear mixed models (LMM). Each rectangle in the clustergram represents the signed -$\log_{10}$-transformed p values from LMM (red, increased in mutant; blue, decreased in mutant). Regions with significant activity differences by LMM ($p < 0.05$) are outlined in yellow. p-values for all homozygous and heterozygous mutants are shown in Figure S4A. For pERK/tERK ratios by region for all fish, see Table S4.

(C) pERK- (top) and merged pERK- and tERK-immunostained brains of *scn1lab*$^{\Delta44/\Delta44}$ and wild-type larvae at 6 dpf. Note the decrease in pERK staining in the mutant forebrain (arrowheads). Dorsal views. FB, forebrain; OT, optic tectum; CB, cerebellum. Scale bar, 50 μm.

(D) Normalized regional activity (pERK/tERK) in *scn1lab*$^{\Delta44/\Delta44}$ (n = 23) and background-matched wild-type (n = 21). ****$p < 0.0001$ (one-way ANOVA).

(E) Voxel-wise *Z* score pERK/tERK values representing brain activity differences in *scn1lab*$^{\Delta44/\Delta44}$ versus background-matched wild-type larvae. Images shown from left to right represent sequential slices: axial views, top row, dorsal to ventral; sagittal views, bottom row, lateral to medial. Scale bar, *Z* score (red/yellow, increased in mutant; cyan/purple, decreased in mutant). Results are shown at $p < 0.05$ whole-brain family-wise error (FWE) corrected with an initial p threshold of 0.0001.

(F) Voxel-wise *Z* score pERK/tERK values representing brain activity differences for the following lines: *dyrk1aa*$^{\Delta77/\Delta77}$*dyrk1ab*$^{\Delta8/\Delta8}$, *chd8*$^{\Delta5/\Delta5}$, *cntnap2a*$^{\Delta121/\Delta121}$*cntnap2b*$^{31ins/31ins}$, *kdm5ba*$^{\Delta17/\Delta17}$*kdm5bb*$^{\Delta14/\Delta14}$, and *tbr1a*$^{\Delta64/\Delta64}$*tbr1b*$^{\Delta10/\Delta10}$. Axial views, top row; sagittal views, bottom row. The horizontal green line in the sagittal view indicates the slice shown in the axial view. Scale bar represents *Z* score (red/yellow, increased in mutant; cyan/purple, decreased in mutant). Results are shown at $p < 0.05$ whole-brain FWE corrected with an initial p threshold of 0.05 for all mutants except *tbr1*, which is not FWE corrected because significance did not meet cluster correction. *tbr1* mutants display significantly decreased activity in the habenula (HB)

(legend continued on next page)

in two mutants with the most robust phenotypes across assays: *scn1lab* and *dyrk1a*. RNA was isolated from whole brains of background-matched homozygous, heterozygous, and wild-type larvae at 6 dpf. Significantly dysregulated pathways were determined by PANTHER Gene Ontology (GO) analysis[48] and gene set enrichment analysis (GSEA) using the Molecular Signatures Database.[49,50] Our analysis identified multiple convergent pathways in *scn1lab* and *dyrk1a* mutants, suggesting shared mechanisms despite their unique brain and behavioral phenotypes. Specifically, GO pathways that are significantly downregulated in both mutants include neurogenesis and neuron differentiation, synaptic signaling, and GABAergic and glutamatergic synapses (Figures 6A and 6B), which overlap with pathways previously implicated in ASDs.[5,10,13] Cell-cycle and mitotic spindle organization pathways are upregulated in *dyrk1a* mutants (Figure 6B), consistent with a known role of *DYRK1A* in cell-cycle regulation.[52] In addition, we found that both upregulated ($p = 1.12 \times 10^{-23}$, Fisher's exact test) and downregulated ($p = 4.34 \times 10^{-49}$) GSEA pathways in *scn1lab* and *dyrk1a* mutants significantly overlap (Figures 6C and 6E). Shared upregulated GSEA pathways include translation and mitochondrial oxidative phosphorylation, which have been implicated in ASDs,[53,54] along with cell-cycle checkpoints, consistent with altered neurogenesis (Figure 6D). Interestingly, estrogen metabolism is also significantly upregulated (Figure 6D), in line with recent studies suggesting modulatory functions of estrogens related to ASD genes.[13,21,55] Unexpectedly, we found that the complement system is significantly upregulated in both mutants (Figure 6D), suggesting neuroimmune dysfunction, which we examine further in the next section. Significantly downregulated GSEA pathways in both mutants include basic neurodevelopmental processes, such as synaptic signaling, cell adhesion molecules, and neurotransmitter release, as well as dopaminergic neurogenesis (Figure 6F), providing a point of overlap with our brain activity findings (Figure 5C). Similar dysregulated pathways were identified in heterozygotes (Figure S6A, Table S6), suggesting moderate gene dosage effects.

We next sought to assess the conservation of dysregulated pathways in zebrafish and mammals using hypothesis-driven GSEA.[56] Our analysis revealed significant enrichment of ASD gene-associated mammalian transcriptomic datasets[8,9,32,51] among dysregulated genes in both zebrafish mutants (Figure 6G, STAR Methods). By comparing differentially expressed (DE) genes in *scn1lab* and *dyrk1a* mutants to human co-expression network modules[8,9] from the BrainSpan dataset,[31] we found that the early and mid-fetal modules from Willsey et al. (2013)[8] and the co-expression modules M13, M16, and M17 from Parikshak et al. (2013)[9] are the most significantly enriched for DE genes (Figure 6G). Interestingly, these modules are the most strongly enriched for ASD gene expression in humans,[8,9] revealing a striking level of conservation downstream of ASD genes in zebrafish and mammals. The co-expression module, M11, which is associated with immune activation,[57] is the most strongly enriched module among upregulated genes in *dyrk1a* mutant brains (Figure 6G), providing additional evidence for neuroimmune dysregulation. In addition, we found that targets of FMRP, the Fragile X mental retardation protein,[51] are significantly enriched among downregulated genes in both mutants, adding to evidence that Fragile X syndrome-associated pathways are disrupted in ASDs.[4] Other ASD genes in the SFARI database[32] are also significantly downregulated in *scn1lab* mutants (Figure 6G). Several intermediate phenotypes were observed in heterozygotes (Figures S6B and S6C). Taken together, our RNA-seq analysis identifies shared molecular pathways in *scn1lab* and *dyrk1a* mutants and demonstrates that ASD gene-associated pathways in zebrafish and mammals are highly conserved.

scn1lab and *dyrk1a* mutants display dopaminergic and microglial abnormalities

To identify cellular mechanisms contributing to dysregulated pathways in *scn1lab* and *dyrk1a* mutants, we performed hypothesis-driven GSEA[56] using cell-type-specific datasets from the mouse brain.[58–60] We found significant enrichment of downregulated genes in neuronal datasets in both *scn1lab* and *dyrk1a* mutants and upregulated genes in an astrocyte-specific dataset[58] in *scn1lab* mutants (Figure 7A), suggesting altered neurogenesis and/or gliogenesis. Next, we found that a dataset of 95 gene candidates, including genes expressed in the mammalian midbrain, Parkinson's disease-associated genes, and known dopaminergic neuron markers, used for single-cell profiling of midbrain dopaminergic neurons in the mouse brain,[60] is significantly enriched for downregulated genes in both mutants (Figure 7A). This provides a striking concordance with our brain activity mapping findings, which also implicate altered dopaminergic signaling. Interestingly, microglia-associated genes from single-cell RNA-seq of the mouse cortex and hippocampus[59] are significantly enriched among upregulated genes in both *scn1lab* and *dyrk1a* mutant brains (Figure 7A), adding to evidence for the dysregulation of neuroimmune pathways. Furthermore, interneuron datasets[59] are significantly enriched for downregulated genes in both mutants (Figure 7A), consistent with the downregulation of GABA-related pathways (Figures 6A-6B and 6F). Pyramidal neuron datasets[59] are also upregulated in *scn1lab* mutants (Figure 7A), consistent with E/I imbalance. As in our RNA-seq pathway analyses, we observed several intermediate phenotypes in heterozygotes (Figure S7A).

To validate cell-type-specific phenotypes, we performed whole-brain immunolabeling in mutant larvae. First, we hypothesized that differences in neurogenesis and/or gliogenesis might be due to abnormal cell proliferation in the developing brain based on the observed dysregulation of cell-cycle pathways (Figures 6B and 6D). To test this hypothesis, we performed whole-brain immunohistochemistry by labeling cells for

(arrowhead) by LMM (B). For the number of animals used in imaging experiments, see STAR Methods (average n = 22–24 per genotype in two to three independent clutches).

(G) Genotype-level p values for each brain region are combined for all homozygous mutants and *cul3a*$^{\Delta 7/\Delta 7}$*cul3b*$^{\Delta 20/+}$, excluding *scn1lab*, using Fisher's method. The scale represents the -$\log_{10}$-transformed combined p value. The thalamus shows the most significant difference in activity ($p = 9.55 \times 10^{-9}$, Fisher's combined probability test).

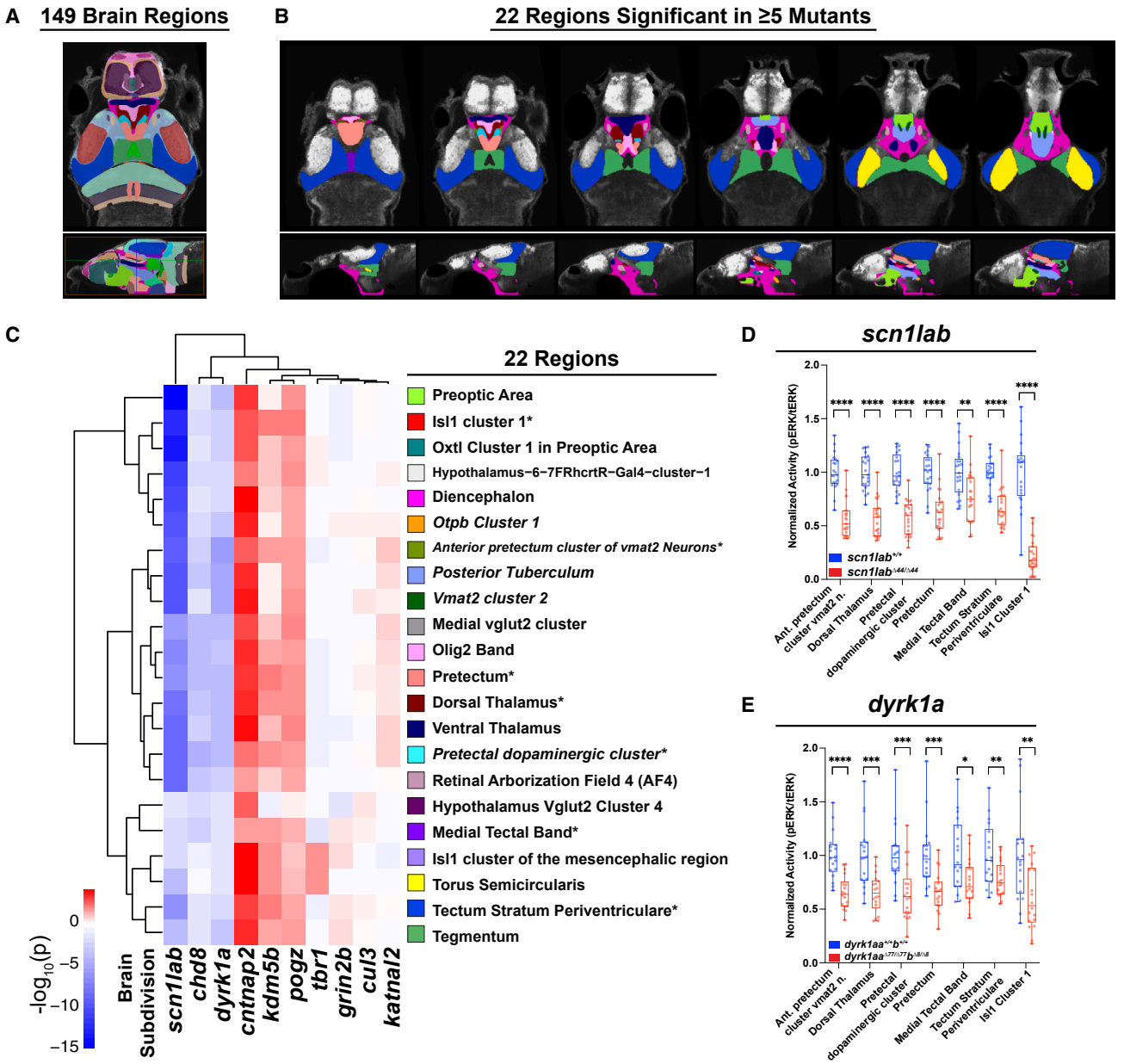

Figure 5. Mutant activity phenotypes converge on 22 brain regions

(A) The 149-region zebrafish brain atlas derived from Randlett et al. (2015).[42]

(B) The 22 regions with significant differences in baseline brain activity in at least five mutants. Region names are shown in (C). Images shown from left to right represent sequential slices: axial views, top row, dorsal to ventral; sagittal views, bottom row, lateral to medial.

(C) Hierarchical clustering of 22 regions with significant differences in baseline brain activity in at least five mutants by linear mixed models (LMM) ($p < 0.05$). Five regions involve dopaminergic signaling (italics): posterior tuberculum, pre-tectal dopaminergic cluster, *vmat2* cluster 2, anterior pretectum cluster of *vmat2* neurons, *otpb* cluster 1. Colors shown to next to each region name refer to (B). *The seven regions with significant differences in baseline activity in at least six mutants (Figures S5B and S5C). Hierarchical clustering of 131 regions with significant differences in activity in at least two mutants by LMM is shown in Figure S5A. For a list of significant regions by mutant, see Table S5.

(D and E) Normalized brain activity (pERK/tERK) in *scn1lab*$^{\Delta 44/\Delta 44}$ (D) and *dyrk1aa*$^{\Delta 77/\Delta 77}$*dyrk1ab*$^{\Delta 8/\Delta 8}$ (E) versus background-matched wild-type fish in the seven brain regions that show significant differences in at least six mutants. Heterozygous phenotypes are shown in Figures S5D and S5E. ****$p < 0.0001$, ***$p < 0.001$, **$p < 0.01$, *$p < 0.05$ (one-way ANOVA).

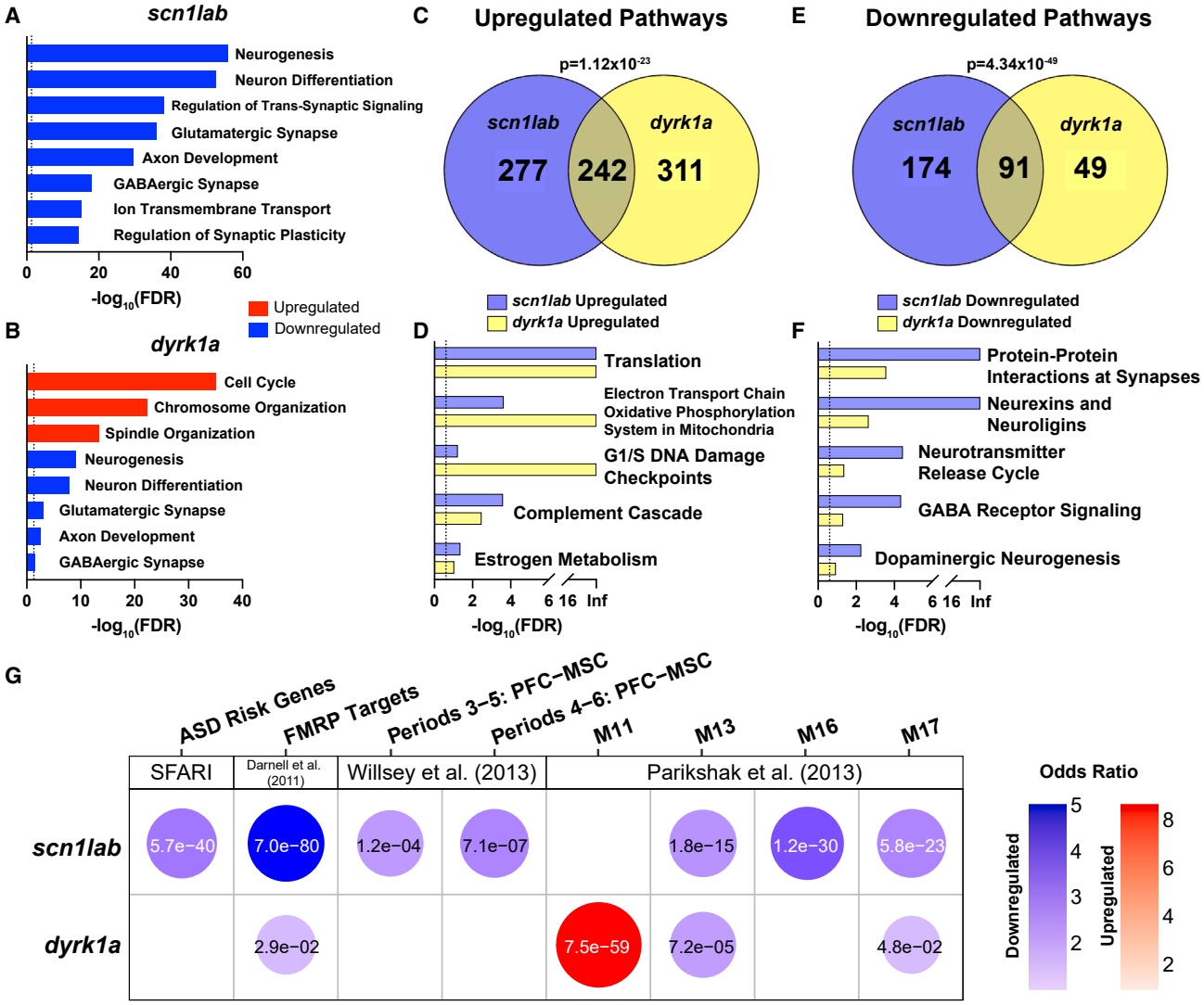

Figure 6. Whole-brain RNA-seq identifies common dysregulated pathways in *scn1lab* and *dyrk1a* mutants

(A and B) Dysregulated GO pathways in *scn1lab*$^{\Delta 44/\Delta 44}$ (A) and *dyrk1aa*$^{\Delta 77/\Delta 77}$*dyrk1ab*$^{\Delta 8/\Delta 8}$ (B) mutants. The dashed line represents FDR of less than 0.05. Pathways enriched in upregulated (red) or downregulated (blue) genes are shown. For a complete list of significant GO pathways, see Table S6.

(C–F) GSEA pathways upregulated (C and D) or downregulated (E and F) in both mutants. The dashed line represents FDR of less than 0.25. p values indicating significant overlap were calculated using Fisher's exact test. For a complete list of significant GSEA pathways, see Table S6.

(G) Hypothesis-driven GSEA of DE genes ($p < 0.1$ and fold-change >1.5) in *scn1lab*$^{\Delta 44/\Delta 44}$ and *dyrk1aa*$^{\Delta 77/\Delta 77}$*dyrk1ab*$^{\Delta 8/\Delta 8}$ mutants using the following datasets: SFARI ASD risk genes,[32] FMRP targets,[51] and human brain co-expression network modules.[8,9] The top four modules from Parikshak et al. (2013)[9] based on combined p value in homozygous mutants using Fisher's method are shown. Gene sets enriched in upregulated (red) or downregulated (blue) genes are shown. Bubbles are shown only for gene sets with significant enrichment ($p < 0.05$). The color intensity and size of each bubble represent the odds ratio. p-values calculated using Fisher's exact test are shown in each bubble. For the complete GSEA including all co-expression network modules in homozygotes and heterozygotes, see Figures S6B and S6C.

phospho-histone H3 (pH3), a marker of proliferative cells. Our analysis showed that pH3$^+$ cells are significantly increased throughout the brain in both mutants (Figures 7B–7D), including regions displaying volume differences, such as the forebrain and optic tectum/midbrain-hindbrain boundary (Figures S7B–S7E). This suggests that early differences in neural cell proliferation might predispose to brain size phenotypes. Next, based on our finding of the downregulation of genes associated with dopaminergic neurogenesis (Figure 6F) and midbrain dopaminergic neurons (Figure 7A), we labeled dopaminergic neurons using an antibody to tyrosine hydroxylase (TH). We found that both *scn1lab* and *dyrk1a* mutants display a significant deficit in TH$^+$ cells in the forebrain (telencephalon), which includes the olfactory bulb and sub-pallium (Figures 7E–7G and S7F–S7J). These differences are more prominent in *scn1lab* mutants, which show a nearly 50% decrease in forebrain dopaminergic neurons (Figures 7E and 7F). There were no significant differences in the number of TH$^+$ cells in the posterior tuberculum

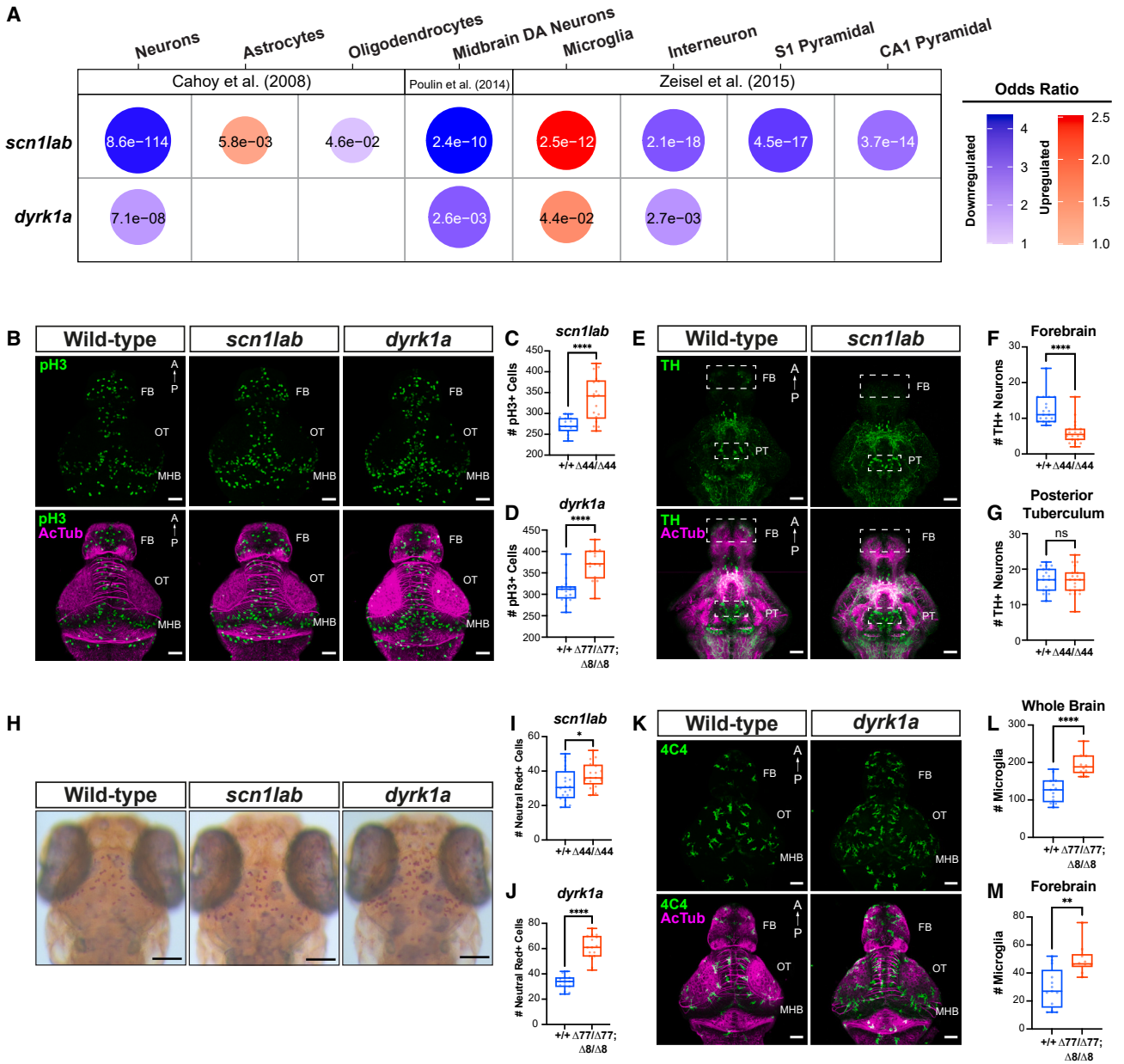

Figure 7. Dopaminergic and microglial phenotypes in *scn1lab* and *dyrk1a* mutants

(A) Hypothesis-driven GSEA of DE genes ($p < 0.1$ and fold-change >1.5) in *scn1lab*$^{\Delta44/\Delta44}$ and *dyrk1aa*$^{\Delta77/\Delta77}$*dyrk1ab*$^{\Delta8/\Delta8}$ mutants using cell-type-specific datasets.[58–60] Cell type markers enriched in upregulated (red) or downregulated (blue) genes are shown. Bubbles are shown only for cell type markers with significant enrichment ($p < 0.05$). The color intensity and size of each bubble represent the odds ratio. p-values calculated using Fisher's exact test are shown in each bubble. For the complete GSEA in homozygotes and heterozygotes, see Figure S7A.

(B) Phospho-histone H3 (pH3, green) and acetylated tubulin (AcTub, magenta) immunostained whole brains of *scn1lab*$^{\Delta44/\Delta44}$ and *dyrk1aa*$^{\Delta77/\Delta77}$*dyrk1ab*$^{\Delta8/\Delta8}$ versus wild-type fish at 3 dpf. Dorsal views. FB, forebrain; OT, optic tectum; MHB, midbrain-hindbrain boundary. Scale bar, 50 μm. For quantification by brain region, see Figures S7B–S7E.

(C and D) Total number of pH3+ cells in *scn1lab*$^{\Delta44/\Delta44}$ (n = 18) versus *scn1lab*$^{+/+}$ (n = 16) (C) and *dyrk1aa*$^{\Delta77/\Delta77}$*dyrk1ab*$^{\Delta8/\Delta8}$ (n = 14) versus wild-type fish (n = 19) (D). ****$p < 0.0001$, one-way ANOVA.

(E) Tyrosine hydroxylase (TH, green) and acetylated tubulin (AcTub, magenta) immunostained whole brains of wild-type, *scn1lab*$^{\Delta44/\Delta44}$, and *dyrk1aa*$^{\Delta77/\Delta77}$*dyrk1ab*$^{\Delta8/\Delta8}$ fish at 4 dpf. Scale bar, 50 μm. Ventral views. FB, forebrain; PT, posterior tuberculum.

(F and G) Total number of TH+ cells in *scn1lab*$^{\Delta44/\Delta44}$ (n = 20) versus *scn1lab*$^{+/+}$ (n = 19) in the forebrain (F) and posterior tuberculum (G) (boxes in [E]). ****$p < 0.0001$, one-way ANOVA. For heterozygous phenotypes, see Figures S7F–S7G.

(H) Neutral red staining of live *scn1lab*$^{\Delta44/\Delta44}$ and *dyrk1aa*$^{\Delta77/\Delta77}$*dyrk1ab*$^{\Delta8/\Delta8}$ versus wild-type fish at 4 dpf. Scale bar, 0.1 mm.

(legend continued on next page)

(Figures 7G and S7J). Overall, these findings suggest that abnormalities in early cell proliferation in the developing brain might lead to altered dopaminergic neuron populations in the forebrain.

To determine the effect of ASD gene LoF on microglial populations, we performed *in vivo* staining of mutant larvae using neutral red, which labels lysosomes as a proxy for microglia.[61] We found a significant increase in neutral red-positive cells in both *dyrk1a* and *scn1lab* mutants (Figures 7H–7J), consistent with the observed upregulation of microglial-associated genes. To validate these findings, we performed whole-brain immunostaining using a microglia-specific antibody.[62] We found a significant increase in microglia in the brains of both mutants (Figures 7K–7M and S7K–S7M). Remarkably, this difference is most prominent in *dyrk1a* mutants, which show a nearly two-fold increase in microglia throughout the brain, including the forebrain (Figures 7K–7M). This suggests that changes in cell proliferation resulting from ASD gene LoF during early brain development might be associated with altered microglial numbers. Taken together, our cell-type-enrichment and whole-brain labeling studies identify dopaminergic and neuroimmune pathways as points of cellular convergence and reveal a prominent role for dysregulated neurogenesis occurring in concert with neuroimmune dysregulation in select ASD gene mutants.

DISCUSSION

This study describes the *in vivo* functional characterization of 10 ASD genes in zebrafish at the behavioral, structural, and circuit levels. Overall, our analysis strongly supports both convergence and divergence across ASD genes. Specifically, we find that each ASD gene mutant displays a unique behavioral, brain size, and activity fingerprint and that no two mutants share identical phenotypes (Figures 2C, 3C and 4B). This suggests that ASD gene LoF broadly impacts basic arousal and sensory processing behaviors, brain size, and baseline brain activity, although not in the same direction or to the same extent. In addition, we find clear evidence for gene dosage effects across modalities, suggesting that haploinsufficiency of ASD genes likely has incremental yet quantifiable effects on multiple phenotypes. Our findings underscore the significant heterogeneity associated with ASDs and are consistent with recent parallel analyses of mouse models of ASD genes and genomic regions.[15,16] These studies also identified a range of brain size and functional connectivity phenotypes, yet defined gene sub-groups with related phenotypes.[15,16] We identified sub-groups of ASD genes with highly correlated behavioral phenotypes (Figure 2H), which would not have been predicted based solely on their known molecular functions. Therefore, our study supports neurosubtyping as an approach to parse out shared biologically relevant features across ASD genes,[63] which may represent a path forward for developing targeted therapeutics as part of a precision medicine approach.

At the same time, our study provides evidence for convergence at multiple levels. For example, we identify the forebrain (telencephalon) and cerebellum as the most significant contributors to brain size phenotypes across mutants (Figure 3H), suggesting that neurogenic regions where ASD genes are highly expressed are particularly vulnerable to ASD gene LoF. Consistent with this finding, we show that cell-cycle and neurogenesis pathways are dysregulated in *dyrk1a* and *scn1lab* mutants, both of which display a reduction in brain volume and an increase in $pH3^+$ mitotic cells. Our results are in line with recent studies highlighting an imbalance of neural proliferation and differentiation in the developing brain, leading to altered neurogenesis and telencephalon size resulting from ASD gene disruption.[12,13] In addition, we find clear evidence for the conservation of molecular mechanisms downstream of ASD genes in zebrafish and mammals, revealing the dysregulation of ASD gene-associated co-expression networks[8,9] and pathways, including synaptic function, FMRP targets, and E/I signaling[5,11,64] in zebrafish mutants, which supports the translatability of our results to mammals. Together, our study supports a central role of ASD genes in controlling neural proliferation and growth of neurogenic regions, which may predispose to altered connectivity in the developing brain.

We also find evidence for convergence at a circuit level, revealing the thalamus as the most significant contributor to brain activity phenotypes across most ASD gene mutants. We identify 22 regions with significant differences in baseline activity in at least one-half of the mutants, which strongly implicates regions involved in sensory-motor regulation, including the dorsal thalamus. Intriguingly, a recent study of social affiliation in zebrafish identified a central role of the dorsal thalamus in a tectothalamic circuit controlling collective social behavior,[65] suggesting that altered baseline activity in this region resulting from ASD gene LoF might lead to social deficits. Our results, therefore, provide additional support for thalamic dysfunction in ASDs[66] and highlight a potential association between disrupted growth of the telencephalon due to ASD gene LoF and altered connectivity in diencephalic regions, which may in turn affect social development. In addition, three lines of evidence indicate that dopaminergic signaling is disrupted in mutants, representing a point of biological convergence. First, dopaminergic regions, such as the posterior tuberculum, are among the top regions showing differences in baseline activity across mutants. Second, a mammalian dopaminergic neuronal dataset is significantly enriched for downregulated genes in *scn1lab* and *dyrk1a* mutants. Third, both mutants display deficits in dopaminergic neurons in the telencephalon. Interestingly, because midbrain dopaminergic systems, such as the VTA, are involved in reward and motivation, dysfunction of these regions has been proposed as a mechanism contributing to social deficits

(I and J) Total number of neutral red+ cells in *scn1lab*$^{\Delta44/\Delta44}$ (n = 17) versus *scn1lab*$^{+/+}$ (n = 20) (I) and *dyrk1aa*$^{\Delta77/\Delta77}$*dyrk1ab*$^{\Delta8/\Delta8}$ (n = 16) versus wild-type fish (n = 15) (J). ****$p < 0.0001$, *$p < 0.05$, one-way ANOVA.

(K) 4C4 (green) and acetylated tubulin (AcTub, magenta) immunostaining of whole brains of *dyrk1aa*$^{\Delta77/\Delta77}$*dyrk1ab*$^{\Delta8/\Delta8}$ and wild-type fish at 4 dpf. Scale bar, 50 μm. Dorsal views. FB, forebrain; OT, optic tectum; MHB, midbrain-hindbrain boundary.

(L and M) Total number of $4C4^+$ cells in *dyrk1aa*$^{\Delta77/\Delta77}$*dyrk1ab*$^{\Delta8/\Delta8}$ (n = 13) versus wild-type (n = 10) in whole brain (L) and forebrain (M). ****$p < 0.0001$, **$p < 0.01$, one-way ANOVA.

in ASDs.[67] Therefore, our study lends additional support to examining the role of neuromodulatory systems in ASDs.

Finally, we report an unexpected point of convergence in neuroimmune pathways. We show that the complement system and microglia-associated genes are enriched among upregulated genes in *scn1lab* and *dyrk1a* mutant brains and identify increased microglia in both mutants, including a nearly two-fold increase in the brains of *dyrk1a* mutants, which also display the most prominent reduction in size. Interestingly, studies of post-mortem brains in individuals with ASDs show an enrichment of microglial genes and an increase in activated microglia,[68–72] illuminating an association of ASDs and neuroimmune dysfunction. Here, we demonstrate a global increase in microglia at stages corresponding to mid-fetal development, providing evidence for early neuroimmune dysfunction in the context of ASD gene LoF. Furthermore, microglia have been shown to play roles in neurogenesis by phagocytosing neural precursor cells[73] and in synaptic pruning[74,75] during brain development. ASD genes are strongly expressed in excitatory and inhibitory neurons[1] and function in cell-cycle control and neurogenesis.[12,13,52,76] This suggests that the increase in microglia in *dyrk1a* and *scn1lab* mutants might occur in response to altered neurogenesis and/or synaptic signaling resulting from gene LoF, though additional studies are needed to determine the extent to which the microglial phenotypes represent a direct or indirect effect of gene disruption and directly contribute to brain size and/or activity phenotypes. Overall, our findings highlight neuroimmune dysfunction in the developing brain as a point of convergence downstream of select ASD genes. Taken together, our study identifies both convergent and divergent effects of ASD gene LoF at multiple neurodevelopmental levels and reveals dopaminergic and neuroimmune pathways as highly relevant to the biology of ASDs.

Limitations of the study

While we identify convergence and divergence across ASD genes and define gene sub-groups at multiple neurodevelopmental levels, additional studies are needed to investigate the extent to which these findings (e.g., behavioral fingerprints) can be leveraged to develop targeted pharmacological treatments using a precision medicine approach. Our findings highlight a central role of the thalamus and dopaminergic regions in baseline brain activity differences in ASD gene mutants, though the mechanisms by which changes in activity in these regions predispose to behavioral alterations remain to be understood. This can be addressed by *in vivo* imaging of these circuits during behavioral tasks. In addition, future studies are needed to determine the mechanisms contributing to alterations in microglial number in *dyrk1a* and *scn1lab* mutants and the extent to which microglial number and/or activation is affected across ASD gene mutants. Finally, examining the brain regions and cell types that we identified in our screen in parallel with mouse and human induced pluripotent stem cell models will be important for translating these findings to mammals and illuminating convergence across systems.

STAR★METHODS

Detailed methods are provided in the online version of this paper and include the following:

SUPPLEMENTAL INFORMATION

Supplemental information can be found online at https://doi.org/10.1016/j.celrep.2023.112243.

ACKNOWLEDGMENTS

We thank P. Hitchcock for the 4C4 antibody; P. de Witte for the *scn1lab*^{didy} line; A.J. Willsey for transcriptome analysis software; A.R. Gupta, T.V. Fernandez, R.J. Muhle, E. Olfson, L. Vitulano, and A. Dettmer for discussions; C. Mariani and T.J. Johnson, Yale DNA Analysis Facility; A. Mennone, Yale Center for Cellular and Molecular Imaging; C. Castaldi, B. Pasqualucci, and E. Sykes, Yale Center for Genome Analysis; R. Garcia Milian, Yale Bioinformatics Support Program; A.G. Ercan-Sencicek for qPCR guidance; and H. Neelakantan for support in software development. This work was supported by the National Institutes of Health R01MH116002, Binational Science Foundation (#2017325), National Genetics Foundation, Simons Foundation (#573508 and #345993), Spector Fund, and Swebilius Foundation (E.J.H.); Kavli Foundation (E.J.H. and P.J.); Wellcome Trust Investigator Award 217150/Z/19/Z (J.R.); Autism Science Foundation (A.P. and K.E.); National Institute of Mental Health (F30MH132282) and the National Institutes of Health Medical Scientist Training Program (T32GM007205) (S.E.F.); the National Institute of Neurological Disorders and Stroke (F31NS130899) and National Institutes of Health Training Program Grant in Genetics (5T32GM007499) (M.C.); Interdepartmental Neuroscience Program at Yale (S.E.F., A.P., D.J., M.C., and I.N.); Vassar College Tananbaum Fellowship (M.Z.); and Yale College Rosenfeld Science Scholars Fellowship, Sherwood E. Silliman Fellowship, and Silliman College Richter Fellowship (K.E.).

AUTHOR CONTRIBUTIONS

H.W.M. and E.J.H. designed the project. E.J.H. generated and characterized zebrafish ASD gene mutants. H.W.M., U.N., S.E.F., T.C., A.P., D.J., P.J., K.D.E., M.C., C. Sakai, B.R., I.N., and E.J.H. performed immunohistochemistry. H.W.M., U.N., T.C., K.D.E., S.I., C. Sakai, C. Szi, B.R., A.G., S.C., M.Z., S.M., and E.J.H. performed behavioral experiments. D.J., U.N., T.C., C.M.L., B.R., X.P., and E.J.H. developed brain mapping pipelines. Y.L., W.W., and Z.W. performed LMM and statistical analysis of behavioral and brain mapping datasets. H.W.M., U.N., K.D.E., C. Szi, and E.J.H. designed *in situ* probes. H.W.M., S.E.F., and K.D.E. performed *in situ* hybridization. H.W.M. and E.J.H. performed qPCR. A.P. performed the zebrafish developmental transcriptome analysis. H.W.M., U.N., S.E.F., T.C., A.P., P.J., M.C., K.D.E., S.I., C. Sakai, C. Szi, B.R., A.G., S.C., and J.M.F. assisted in screening mutant lines, genotyping, and zebrafish husbandry. H.W.M. and S.E.F. performed RNA sequencing. Y.L., N.L., D.Z., and Z.W. analyzed RNA sequencing datasets. S.I., C. Szi, and E.J.H. developed the paradigm and B.V.W. developed software for visual-startle assays. J.W. assisted in behavioral analyses. J.E. developed software for behavioral analyses. M.G. and J.R. provided software and assistance in the analysis of sleep-wake phenotypes. H.W.M., S.E.F., A.P., and P.J. performed neutral red staining and quantification. H.W.M., U.N., and S.E.F. quantified immunostaining datasets. H.W.M. and E.J.H. wrote the manuscript with input from U.N., Y.L., S.E.F., A.P., P.J., C.M.L., D.Z., M.C., J.R., X.P., and Z.W.

DECLARATION OF INTERESTS

X.P. is a consultant for the Brain Electrophysiology Laboratory Company.

INCLUSION AND DIVERSITY

One or more of the authors of this paper self-identifies as an under represented ethnic minority in their field of research or within their geographical location. One or more of the authors of this paper self-identifies as living with a disability. One or more of the authors of this paper received support from a program designed to increase minority representation in their field of research.

Received: July 5, 2022
Revised: November 15, 2022
Accepted: February 23, 2023

REFERENCES

1. Satterstrom, F.K., Kosmicki, J.A., Wang, J., Breen, M.S., De Rubeis, S., An, J.Y., Peng, M., Collins, R., Grove, J., Klei, L., et al. (2020). Large-scale exome sequencing study implicates both developmental and functional changes in the neurobiology of autism. Cell *180*, 568–584.e23. https://doi.org/10.1016/j.cell.2019.12.036.
2. Wang, T., Hoekzema, K., Vecchio, D., Wu, H., Sulovari, A., Coe, B.P., Gillentine, M.A., Wilfert, A.B., Perez-Jurado, L.A., Kvarnung, M., et al. (2020). Large-scale targeted sequencing identifies risk genes for neurodevelopmental disorders. Nat. Commun. *11*, 4932. https://doi.org/10.1038/s41467-020-18723-y.
3. Sanders, S.J., He, X., Willsey, A.J., Ercan-Sencicek, A.G., Samocha, K.E., Cicek, A.E., Murtha, M.T., Bal, V.H., Bishop, S.L., Dong, S., et al. (2015). Insights into autism spectrum disorder genomic architecture and biology from 71 risk loci. Neuron *87*, 1215–1233. https://doi.org/10.1016/j.neuron.2015.09.016.
4. Iossifov, I., O'Roak, B.J., Sanders, S.J., Ronemus, M., Krumm, N., Levy, D., Stessman, H.A., Witherspoon, K.T., Vives, L., Patterson, K.E., et al. (2014). The contribution of de novo coding mutations to autism spectrum disorder. Nature *515*, 216–221. https://doi.org/10.1038/nature13908.
5. De Rubeis, S., He, X., Goldberg, A.P., Poultney, C.S., Samocha, K., Cicek, A.E., Kou, Y., Liu, L., Fromer, M., Walker, S., et al. (2014). Synaptic, transcriptional and chromatin genes disrupted in autism. Nature *515*, 209–215. https://doi.org/10.1038/nature13772.
6. Sestan, N., and State, M.W. (2018). Lost in translation: traversing the complex path from genomics to therapeutics in autism spectrum disorder. Neuron *100*, 406–423. https://doi.org/10.1016/j.neuron.2018.10.015.
7. Willsey, H.R., Willsey, A.J., Wang, B., and State, M.W. (2022). Genomics, convergent neuroscience and progress in understanding autism spectrum disorder. Nat. Rev. Neurosci. *23*, 323–341. https://doi.org/10.1038/s41583-022-00576-7.
8. Willsey, A.J., Sanders, S.J., Li, M., Dong, S., Tebbenkamp, A.T., Muhle, R.A., Reilly, S.K., Lin, L., Fertuzinhos, S., Miller, J.A., et al. (2013). Coexpression networks implicate human midfetal deep cortical projection neurons in the pathogenesis of autism. Cell *155*, 997–1007. https://doi.org/10.1016/j.cell.2013.10.020.
9. Parikshak, N.N., Luo, R., Zhang, A., Won, H., Lowe, J.K., Chandran, V., Horvath, S., and Geschwind, D.H. (2013). Integrative functional genomic analyses implicate specific molecular pathways and circuits in autism. Cell *155*, 1008–1021. https://doi.org/10.1016/j.cell.2013.10.031.
10. Rubenstein, J.L.R., and Merzenich, M.M. (2003). Model of autism: increased ratio of excitation/inhibition in key neural systems. Genes Brain Behav. *2*, 255–267.
11. Paulsen, B., Velasco, S., Kedaigle, A.J., Pigoni, M., Quadrato, G., Deo, A.J., Adiconis, X., Uzquiano, A., Sartore, R., Yang, S.M., et al. (2022). Autism genes converge on asynchronous development of shared neuron classes. Nature *602*, 268–273. https://doi.org/10.1038/s41586-021-04358-6.
12. Durak, O., Gao, F., Kaeser-Woo, Y.J., Rueda, R., Martorell, A.J., Nott, A., Liu, C.Y., Watson, L.A., and Tsai, L.H. (2016). Chd8 mediates cortical neurogenesis via transcriptional regulation of cell cycle and Wnt signaling. Nat. Neurosci. *19*, 1477–1488. https://doi.org/10.1038/nn.4400.
13. Willsey, H.R., Exner, C.R.T., Xu, Y., Everitt, A., Sun, N., Wang, B., Dea, J., Schmunk, G., Zaltsman, Y., Teerikorpi, N., et al. (2021). Parallel in vivo analysis of large-effect autism genes implicates cortical neurogenesis and estrogen in risk and resilience. Neuron *109*, 1409. https://doi.org/10.1016/j.neuron.2021.03.030.
14. Jin, X., Simmons, S.K., Guo, A., Shetty, A.S., Ko, M., Nguyen, L., Jokhi, V., Robinson, E., Oyler, P., Curry, N., et al. (2020). In vivo Perturb-Seq reveals neuronal and glial abnormalities associated with autism risk genes. Science *370*, eaaz6063. https://doi.org/10.1126/science.aaz6063.
15. Zerbi, V., Pagani, M., Markicevic, M., Matteoli, M., Pozzi, D., Fagiolini, M., Bozzi, Y., Galbusera, A., Scattoni, M.L., Provenzano, G., et al. (2021). Brain mapping across 16 autism mouse models reveals a spectrum of functional connectivity subtypes. Mol. Psychiatry *26*, 7610–7620. https://doi.org/10.1038/s41380-021-01245-4.
16. Ellegood, J., Anagnostou, E., Babineau, B.A., Crawley, J.N., Lin, L., Genestine, M., DiCicco-Bloom, E., Lai, J.K.Y., Foster, J.A., Peñagarikano, O., et al. (2015). Clustering autism: using neuroanatomical differences in 26 mouse models to gain insight into the heterogeneity. Mol. Psychiatry *20*, 118–125. https://doi.org/10.1038/mp.2014.98.
17. McCammon, J.M., and Sive, H. (2015). Challenges in understanding psychiatric disorders and developing therapeutics: a role for zebrafish. Dis. Model. Mech. *8*, 647–656. https://doi.org/10.1242/dmm.019620.
18. Ijaz, S., and Hoffman, E.J. (2016). Zebrafish: a translational model system for studying neuropsychiatric disorders. J. Am. Acad. Child Adolesc. Psychiatry *55*, 746–748. https://doi.org/10.1016/j.jaac.2016.06.008.
19. Sakai, C., Ijaz, S., and Hoffman, E.J. (2018). Zebrafish models of neurodevelopmental disorders: past, present, and future. Front. Mol. Neurosci. *11*, 294. https://doi.org/10.3389/fnmol.2018.00294.
20. Kozol, R.A., Abrams, A.J., James, D.M., Buglo, E., Yan, Q., and Dallman, J.E. (2016). Function over form: modeling groups of inherited neurological conditions in zebrafish. Front. Mol. Neurosci. *9*, 55. https://doi.org/10.3389/fnmol.2016.00055.
21. Hoffman, E.J., Turner, K.J., Fernandez, J.M., Cifuentes, D., Ghosh, M., Ijaz, S., Jain, R.A., Kubo, F., Bill, B.R., Baier, H., et al. (2016). Estrogens

suppress a behavioral phenotype in zebrafish mutants of the autism risk gene, CNTNAP2. Neuron *89*, 725–733. https://doi.org/10.1016/j.neuron.2015.12.039.

22. Thyme, S.B., Pieper, L.M., Li, E.H., Pandey, S., Wang, Y., Morris, N.S., Sha, C., Choi, J.W., Herrera, K.J., Soucy, E.R., et al. (2019). Phenotypic landscape of schizophrenia-associated genes defines candidates and their shared functions. Cell *177*, 478–491.e20. https://doi.org/10.1016/j.cell.2019.01.048.
23. Guo, S. (2009). Using zebrafish to assess the impact of drugs on neural development and function. Expert Opin. Drug Discov. *4*, 715–726. https://doi.org/10.1517/17460440902988464.
24. Rihel, J., Prober, D.A., Arvanites, A., Lam, K., Zimmerman, S., Jang, S., Haggarty, S.J., Kokel, D., Rubin, L.L., Peterson, R.T., and Schier, A.F. (2010). Zebrafish behavioral profiling links drugs to biological targets and rest/wake regulation. Science *327*, 348–351. https://doi.org/10.1126/science.1183090.
25. Lovett-Barron, M., Andalman, A.S., Allen, W.E., Vesuna, S., Kauvar, I., Burns, V.M., and Deisseroth, K. (2017). Ancestral circuits for the coordinated modulation of brain state. Cell *171*, 1411–1423.e17. https://doi.org/10.1016/j.cell.2017.10.021.
26. Burgess, H.A., and Granato, M. (2007). Modulation of locomotor activity in larval zebrafish during light adaptation. J. Exp. Biol. *210*, 2526–2539. https://doi.org/10.1242/jeb.003939.
27. Burgess, H.A., and Granato, M. (2007). Sensorimotor gating in larval zebrafish. J. Neurosci. *27*, 4984–4994. https://doi.org/10.1523/JNEUROSCI.0615-07.2007.
28. Schoonheim, P.J., Arrenberg, A.B., Del Bene, F., and Baier, H. (2010). Optogenetic localization and genetic perturbation of saccade-generating neurons in zebrafish. J. Neurosci. *30*, 7111–7120. https://doi.org/10.1523/JNEUROSCI.5193-09.2010.
29. Prober, D.A., Rihel, J., Onah, A.A., Sung, R.J., and Schier, A.F. (2006). Hypocretin/orexin overexpression induces an insomnia-like phenotype in zebrafish. J. Neurosci. *26*, 13400–13410. https://doi.org/10.1523/JNEUROSCI.4332-06.2006.
30. White, R.J., Collins, J.E., Sealy, I.M., Wali, N., Dooley, C.M., Digby, Z., Stemple, D.L., Murphy, D.N., Billis, K., lier, T., et al. (2017). A high-resolution mRNA expression time course of embryonic development in zebrafish. Elife *6*, e30860. https://doi.org/10.7554/eLife.30860.
31. Kang, H.J., Kawasawa, Y.I., Cheng, F., Zhu, Y., Xu, X., Li, M., Sousa, A.M.M., Pletikos, M., Meyer, K.A., Sedmak, G., et al. (2011). Spatio-temporal transcriptome of the human brain. Nature *478*, 483–489. https://doi.org/10.1038/nature10523.
32. SFARI Gene. (2022).[updated 11 Jan 2022; accessed 30 April 2022] https://gene.sfari.org/
33. Schmidt, R., Strähle, U., and Scholpp, S. (2013). Neurogenesis in zebrafish - from embryo to adult. Neural Dev. *8*, 3. https://doi.org/10.1186/1749-8104-8-3.
34. Scott, C.A., Marsden, A.N., and Slusarski, D.C. (2016). Automated, high-throughput, in vivo analysis of visual function using the zebrafish. Developmental Dynamics *245*, 605–613. https://doi.org/10.1002/dvdy.24398.
35. Méjécase, C., Way, C.M., Owen, N., and Moosajee, M. (2021). Ocular phenotype associated with DYRK1A variants. Genes *12*, 234. https://doi.org/10.3390/genes12020234.
36. Verbeek, N., Kasteleijn-Nolst Trenité, D., Wassenaar, M., van Campen, J., Sonsma, A., Gunning, W.B., de Weerd, A., Knoers, N., Spetgens, W., Gutter, T., et al. (2017). Photosensitivity in Dravet syndrome is under-recognized and related to prognosis. Clin. Neurophysiol. *128*, 323–330. https://doi.org/10.1016/j.clinph.2016.11.021.
37. van Bon, B.W.M., Coe, B.P., Bernier, R., Green, C., Gerdts, J., Witherspoon, K., Kleefstra, T., Willemsen, M.H., Kumar, R., Bosco, P., et al. (2016). Disruptive de novo mutations of DYRK1A lead to a syndromic form of autism and ID. Mol. Psychiatry *21*, 126–132. https://doi.org/10.1038/mp.2015.5.
38. Van Nuland, A., Ivanenko, A., Meskis, M.A., Villas, N., Knupp, K.G., and Berg, A.T. (2021). Sleep in Dravet syndrome: a parent-driven survey. Seizure *85*, 102–110. https://doi.org/10.1016/j.seizure.2020.12.021.
39. Coll-Tané, M., Gong, N.N., Belfer, S.J., van Renssen, L.V., Kurtz-Nelson, E.C., Szuperak, M., Eidhof, I., van Reijmersdal, B., Terwindt, I., Durkin, J., et al. (2021). The CHD8/CHD7/Kismet family links blood-brain barrier glia and serotonin to ASD-associated sleep defects. Sci. Adv. *7*, eabe2626. https://doi.org/10.1126/sciadv.abe2626.
40. Yook, C., Kim, K., Kim, D., Kang, H., Kim, S.G., Kim, E., and Kim, S.Y. (2019). A TBR1-K228E mutation induces Tbr1 upregulation, altered cortical distribution of interneurons, increased inhibitory synaptic transmission, and autistic-like behavioral deficits in mice. Front. Mol. Neurosci. *12*, 241. https://doi.org/10.3389/fnmol.2019.00241.
41. Courchesne, E., Campbell, K., and Solso, S. (2011). Brain growth across the life span in autism: age-specific changes in anatomical pathology. Brain Res. *1380*, 138–145. https://doi.org/10.1016/j.brainres.2010.09.101.
42. Randlett, O., Wee, C.L., Naumann, E.A., Nnaemeka, O., Schoppik, D., Fitzgerald, J.E., Portugues, R., Lacoste, A.M.B., Riegler, C., Engert, F., and Schier, A.F. (2015). Whole-brain activity mapping onto a zebrafish brain atlas. Nat. Methods *12*, 1039–1046. https://doi.org/10.1038/nmeth.3581.
43. Levy, J.A., LaFlamme, C.W., Tsaprailis, G., Crynen, G., and Page, D.T. (2021). Dyrk1a mutations cause undergrowth of cortical pyramidal neurons via dysregulated growth factor signaling. Biol. Psychiatry *90*, 295–306. https://doi.org/10.1016/j.biopsych.2021.01.012.
44. Tejedor, F., Zhu, X.R., Kaltenbach, E., Ackermann, A., Baumann, A., Canal, I., Heisenberg, M., Fischbach, K.F., and Pongs, O. (1995). minibrain: a new protein kinase family involved in postembryonic neurogenesis in Drosophila. Neuron *14*, 287–301. https://doi.org/10.1016/0896-6273(95)90286-4.
45. Wen, L., Wei, W., Gu, W., Huang, P., Ren, X., Zhang, Z., Zhu, Z., Lin, S., and Zhang, B. (2008). Visualization of monoaminergic neurons and neurotoxicity of MPTP in live transgenic zebrafish. Dev. Biol. *314*, 84–92. https://doi.org/10.1016/j.ydbio.2007.11.012.
46. Ryu, S., Mahler, J., Acampora, D., Holzschuh, J., Erhardt, S., Omodei, D., Simeone, A., and Driever, W. (2007). Orthopedia homeodomain protein is essential for diencephalic dopaminergic neuron development. Curr. Biol. *17*, 873–880. https://doi.org/10.1016/j.cub.2007.04.003.
47. Rink, E., and Wullimann, M.F. (2001). The teleostean (zebrafish) dopaminergic system ascending to the subpallium (striatum) is located in the basal diencephalon (posterior tuberculum). Brain Res. *889*, 316–330. https://doi.org/10.1016/s0006-8993(00)03174-7.
48. Thomas, P.D., Campbell, M.J., Kejariwal, A., Mi, H., Karlak, B., Daverman, R., Diemer, K., Muruganujan, A., and Narechania, A. (2003). PANTHER: a library of protein families and subfamilies indexed by function. Genome Res. *13*, 2129–2141. https://doi.org/10.1101/gr.772403.
49. Subramanian, A., Tamayo, P., Mootha, V.K., Mukherjee, S., Ebert, B.L., Gillette, M.A., Paulovich, A., Pomeroy, S.L., Golub, T.R., Lander, E.S., and Mesirov, J.P. (2005). Gene set enrichment analysis: a knowledge-based approach for interpreting genome-wide expression profiles. Proc. Natl. Acad. Sci. USA *102*, 15545–15550. https://doi.org/10.1073/pnas.0506580102.
50. Mootha, V.K., Lindgren, C.M., Eriksson, K.F., Subramanian, A., Sihag, S., Lehar, J., Puigserver, P., Carlsson, E., Ridderstråle, M., Laurila, E., et al. (2003). PGC-1alpha-responsive genes involved in oxidative phosphorylation are coordinately downregulated in human diabetes. Nat. Genet. *34*, 267–273. https://doi.org/10.1038/ng1180.
51. Darnell, J.C., Van Driesche, S.J., Zhang, C., Hung, K.Y.S., Mele, A., Fraser, C.E., Stone, E.F., Chen, C., Fak, J.J., Chi, S.W., et al. (2011). FMRP stalls ribosomal translocation on mRNAs linked to synaptic function and autism. Cell *146*, 247–261. https://doi.org/10.1016/j.cell.2011.06.013.
52. Willsey, H.R., Xu, Y., Everitt, A., Dea, J., Exner, C.R.T., Willsey, A.J., State, M.W., and Harland, R.M. (2020). The neurodevelopmental disorder risk gene DYRK1A is required for ciliogenesis and control of brain size in

Xenopus embryos. Development *147*, dev189290. https://doi.org/10.1242/dev.189290.

53. Kelleher, R.J., 3rd, and Bear, M.F. (2008). The autistic neuron: troubled translation? Cell *135*, 401–406. https://doi.org/10.1016/j.cell.2008.10.017.
54. Hollis, F., Kanellopoulos, A.K., and Bagni, C. (2017). Mitochondrial dysfunction in Autism Spectrum Disorder: clinical features and perspectives. Curr. Opin. Neurobiol. *45*, 178–187. https://doi.org/10.1016/j.conb.2017.05.018.
55. Gegenhuber, B., Wu, M.V., Bronstein, R., and Tollkuhn, J. (2022). Gene regulation by gonadal hormone receptors underlies brain sex differences. Nature *606*, 153–159. https://doi.org/10.1038/s41586-022-04686-1.
56. Werling, D.M., Parikshak, N.N., and Geschwind, D.H. (2016). Gene expression in human brain implicates sexually dimorphic pathways in autism spectrum disorders. Nat. Commun. *7*, 10717. https://doi.org/10.1038/ncomms10717.
57. Kimura, R., Swarup, V., Tomiwa, K., Gandal, M.J., Parikshak, N.N., Funabiki, Y., Nakata, M., Awaya, T., Kato, T., Iida, K., et al. (2019). Integrative network analysis reveals biological pathways associated with Williams syndrome. J. Child Psychol. Psychiatry *60*, 585–598. https://doi.org/10.1111/jcpp.12999.
58. Cahoy, J.D., Emery, B., Kaushal, A., Foo, L.C., Zamanian, J.L., Christopherson, K.S., Xing, Y., Lubischer, J.L., Krieg, P.A., Krupenko, S.A., et al. (2008). A transcriptome database for astrocytes, neurons, and oligodendrocytes: a new resource for understanding brain development and function. J. Neurosci. *28*, 264–278. https://doi.org/10.1523/JNEUROSCI.4178-07.2008.
59. Zeisel, A., Muñoz-Manchado, A.B., Codeluppi, S., Lönnerberg, P., La Manno, G., Juréus, A., Marques, S., Munguba, H., He, L., Betsholtz, C., et al. (2015). Brain structure. Cell types in the mouse cortex and hippocampus revealed by single-cell RNA-seq. Science *347*, 1138–1142. https://doi.org/10.1126/science.aaa1934.
60. Poulin, J.F., Zou, J., Drouin-Ouellet, J., Kim, K.Y.A., Cicchetti, F., and Awatramani, R.B. (2014). Defining midbrain dopaminergic neuron diversity by single-cell gene expression profiling. Cell Rep. *9*, 930–943. https://doi.org/10.1016/j.celrep.2014.10.008.
61. Herbomel, P., Thisse, B., and Thisse, C. (2001). Zebrafish early macrophages colonize cephalic mesenchyme and developing brain, retina, and epidermis through a M-CSF receptor-dependent invasive process. Dev. Biol. *238*, 274–288. https://doi.org/10.1006/dbio.2001.0393.
62. Raymond, P.A., Barthel, L.K., Bernardos, R.L., and Perkowski, J.J. (2006). Molecular characterization of retinal stem cells and their niches in adult zebrafish. BMC Dev. Biol. *6*, 36. https://doi.org/10.1186/1471-213X-6-36.
63. Hong, S.J., Vogelstein, J.T., Gozzi, A., Bernhardt, B.C., Yeo, B.T.T., Milham, M.P., and Di Martino, A. (2020). Toward neurosubtypes in autism. Biol. Psychiatry *88*, 111–128. https://doi.org/10.1016/j.biopsych.2020.03.022.
64. Iossifov, I., Ronemus, M., Levy, D., Wang, Z., Hakker, I., Rosenbaum, J., Yamrom, B., Lee, Y.H., Narzisi, G., Leotta, A., et al. (2012). De novo gene disruptions in children on the autistic spectrum. Neuron *74*, 285–299. https://doi.org/10.1016/j.neuron.2012.04.009.
65. Kappel, J.M., Förster, D., Slangewal, K., Shainer, I., Svara, F., Donovan, J.C., Sherman, S., Januszewski, M., Baier, H., and Larsch, J. (2022). Visual recognition of social signals by a tectothalamic neural circuit. Nature *608*, 146–152. https://doi.org/10.1038/s41586-022-04925-5.
66. Moreau, C.A., Urchs, S.G.W., Kuldeep, K., Orban, P., Schramm, C., Dumas, G., Labbe, A., Huguet, G., Douard, E., Quirion, P.O., et al. (2020). Mutations associated with neuropsychiatric conditions delineate functional brain connectivity dimensions contributing to autism and schizophrenia. Nat. Commun. *11*, 5272. https://doi.org/10.1038/s41467-020-18997-2.
67. Pavăl, D. (2017). A dopamine hypothesis of autism spectrum disorder. Dev. Neurosci. *39*, 355–360. https://doi.org/10.1159/000478725.
68. Voineagu, I., Wang, X., Johnston, P., Lowe, J.K., Tian, Y., Horvath, S., Mill, J., Cantor, R.M., Blencowe, B.J., and Geschwind, D.H. (2011). Transcriptomic analysis of autistic brain reveals convergent molecular pathology. Nature *474*, 380–384. https://doi.org/10.1038/nature10110.
69. Velmeshev, D., Schirmer, L., Jung, D., Haeussler, M., Perez, Y., Mayer, S., Bhaduri, A., Goyal, N., Rowitch, D.H., and Kriegstein, A.R. (2019). Single-cell genomics identifies cell type-specific molecular changes in autism. Science *364*, 685–689. https://doi.org/10.1126/science.aav8130.
70. Gupta, S., Ellis, S.E., Ashar, F.N., Moes, A., Bader, J.S., Zhan, J., West, A.B., and Arking, D.E. (2014). Transcriptome analysis reveals dysregulation of innate immune response genes and neuronal activity-dependent genes in autism. Nat. Commun. *5*, 5748. https://doi.org/10.1038/ncomms6748.
71. Lee, A.S., Azmitia, E.C., and Whitaker-Azmitia, P.M. (2017). Developmental microglial priming in postmortem autism spectrum disorder temporal cortex. Brain Behav. Immun. *62*, 193–202. https://doi.org/10.1016/j.bbi.2017.01.019.
72. Vargas, D.L., Nascimbene, C., Krishnan, C., Zimmerman, A.W., and Pardo, C.A. (2005). Neuroglial activation and neuroinflammation in the brain of patients with autism. Ann. Neurol. *57*, 67–81. https://doi.org/10.1002/ana.20315.
73. Cunningham, C.L., Martínez-Cerdeño, V., and Noctor, S.C. (2013). Microglia regulate the number of neural precursor cells in the developing cerebral cortex. J. Neurosci. *33*, 4216–4233. https://doi.org/10.1523/JNEUROSCI.3441-12.2013.
74. Paolicelli, R.C., Bolasco, G., Pagani, F., Maggi, L., Scianni, M., Panzanelli, P., Giustetto, M., Ferreira, T.A., Guiducci, E., Dumas, L., et al. (2011). Synaptic pruning by microglia is necessary for normal brain development. Science *333*, 1456–1458. https://doi.org/10.1126/science.1202529.
75. Schafer, D.P., Lehrman, E.K., Kautzman, A.G., Koyama, R., Mardinly, A.R., Yamasaki, R., Ransohoff, R.M., Greenberg, M.E., Barres, B.A., and Stevens, B. (2012). Microglia sculpt postnatal neural circuits in an activity and complement-dependent manner. Neuron *74*, 691–705. https://doi.org/10.1016/j.neuron.2012.03.026.
76. Lalli, M.A., Avey, D., Dougherty, J.D., Milbrandt, J., and Mitra, R.D. (2020). High-throughput single-cell functional elucidation of neurodevelopmental disease-associated genes reveals convergent mechanisms altering neuronal differentiation. Genome Res. *30*, 1317–1331. https://doi.org/10.1101/gr.262295.120.
77. Kroll, F., Powell, G.T., Ghosh, M., Gestri, G., Antinucci, P., Hearn, T.J., Tunbak, H., Lim, S., Dennis, H.W., Fernandez, J.M., et al. (2021). A simple and effective f0 knockout method for rapid screening of behaviour and other complex phenotypes. Elife *10*. https://doi.org/10.7554/eLife.59683.
78. Madeira, F., Pearce, M., Tivey, A.R.N., Basutkar, P., Lee, J., Edbali, O., Madhusoodanan, N., Kolesnikov, A., and Lopez, R. (2022). Search and sequence analysis tools services from EMBL-EBI in 2022. Nucleic Acids Res. *50*, W276–W279. https://doi.org/10.1093/nar/gkac240.
79. Sander, J.D., Zaback, P., Joung, J.K., Voytas, D.F., and Dobbs, D. (2007). Zinc Finger Targeter (ZiFiT): an engineered zinc finger/target site design tool. Nucleic Acids Res. *35*, W599–W605. https://doi.org/10.1093/nar/gkm349.
80. Sander, J.D., Maeder, M.L., Reyon, D., Voytas, D.F., Joung, J.K., and Dobbs, D. (2010). ZiFiT (Zinc Finger Targeter): an updated zinc finger engineering tool. Nucleic Acids Res. *38*, W462–W468. https://doi.org/10.1093/nar/gkq319.
81. Moreno-Mateos, M.A., Vejnar, C.E., Beaudoin, J.D., Fernandez, J.P., Mis, E.K., Khokha, M.K., and Giraldez, A.J. (2015). CRISPRscan: designing highly efficient sgRNAs for CRISPR-Cas9 targeting in vivo. Nat. Methods *12*, 982–988. https://doi.org/10.1038/nmeth.3543.
82. Dahlem, T.J., Hoshijima, K., Jurynec, M.J., Gunther, D., Starker, C.G., Locke, A.S., Weis, A.M., Voytas, D.F., and Grunwald, D.J. (2012). Simple methods for generating and detecting locus-specific mutations induced with TALENs in the zebrafish genome. PLoS Genet. *8*, e1002861. https://doi.org/10.1371/journal.pgen.1002861.

83. Thisse, C., Thisse, B., Schilling, T.F., and Postlethwait, J.H. (1993). Structure of the zebrafish snail1 gene and its expression in wild-type, spadetail and no tail mutant embryos. Development *119*, 1203–1215.

84. Yates, A., Akanni, W., Amode, M.R., Barrell, D., Billis, K., Carvalho-Silva, D., Cummins, C., Clapham, P., Fitzgerald, S., Gil, L., et al. (2016). Ensembl 2016. Nucleic Acids Res. *44*, D710–D716. https://doi.org/10.1093/nar/gkv1157.

85. Zheng, J., Long, F., Cao, X., Xiong, B., and Li, Y. (2022). Knockout of Katnal2 leads to autism-like behaviors and developmental delay in zebrafish. Int. J. Mol. Sci. *23*, 8389. https://doi.org/10.3390/ijms23158389.

86. Bradford, Y.M., Van Slyke, C.E., Ruzicka, L., Singer, A., Eagle, A., Fashena, D., Howe, D.G., Frazer, K., Martin, R., Paddock, H., et al. (2022). Zebrafish information network, the knowledgebase for danio rerio research. Genetics *220*. https://doi.org/10.1093/genetics/iyac016.

87. Wilson, S.W., Ross, L.S., Parrett, T., and Easter, S.S., Jr. (1990). The development of a simple scaffold of axon tracts in the brain of the embryonic zebrafish. Development *108*, 121–145.

88. Schindelin, J., Arganda-Carreras, I., Frise, E., Kaynig, V., Longair, M., Pietzsch, T., Preibisch, S., Rueden, C., Saalfeld, S., Schmid, B., et al. (2012). Fiji: an open-source platform for biological-image analysis. Nat. Methods *9*, 676–682. https://doi.org/10.1038/nmeth.2019.

89. Sallinen, V., Torkko, V., Sundvik, M., Reenilä, I., Khrustalyov, D., Kaslin, J., and Panula, P. (2009). MPTP and MPP+ target specific aminergic cell populations in larval zebrafish. J. Neurochem. *108*, 719–731. https://doi.org/10.1111/j.1471-4159.2008.05793.x.

90. Nunes, A.R., Gliksberg, M., Varela, S.A.M., Teles, M., Wircer, E., Blechman, J., Petri, G., Levkowitz, G., and Oliveira, R.F. (2021). Developmental effects of oxytocin neurons on social affiliation and processing of social information. J. Neurosci. *41*, 8742–8760. https://doi.org/10.1523/JNEUROSCI.2939-20.2021.

91. BioImage Suite Web. https://bioimagesuiteweb.github.io/webapp/.

92. Staib, L.H., Jackowski, M., and Papademetris, X. (2006). Brain shape characterization from deformation. Proc. IEEE Int. Symp. Biomed. Imaging *3*, 1140–1143.

93. Najt, P., Wang, F., Spencer, L., Johnston, J.A.Y., Cox Lippard, E.T., Pittman, B.P., Lacadie, C., Staib, L.H., Papademetris, X., and Blumberg, H.P. (2016). Anterior cortical development during adolescence in bipolar disorder. Biol. Psychiatry *79*, 303–310. https://doi.org/10.1016/j.biopsych.2015.03.026.

94. Cox, R.W. (1996). AFNI: software for analysis and visualization of functional magnetic resonance neuroimages. Comput. Biomed. Res. *29*, 162–173. https://doi.org/10.1006/cbmr.1996.0014.

95. Harrer, M., Cuijpers, P., Furukawa, T.A., and Ebert, D.D. (2021). Doing Meta-Analysis with R: A Hands-On Guide (Chapmann & Hall/CRC Press).

96. Kim, D., Paggi, J.M., Park, C., Bennett, C., and Salzberg, S.L. (2019). Graph-based genome alignment and genotyping with HISAT2 and HISAT-genotype. Nat. Biotechnol. *37*, 907–915. https://doi.org/10.1038/s41587-019-0201-4.

97. Pertea, M., Pertea, G.M., Antonescu, C.M., Chang, T.-C., Mendell, J.T., and Salzberg, S.L. (2015). StringTie enables improved reconstruction of a transcriptome from RNA-seq reads. Nat. Biotechnol. *33*, 290–295. https://doi.org/10.1038/nbt.3122 http://www.nature.com/nbt/journal/v33/n3/abs/nbt.3122.html#supplementary-information.

98. Love, M.I., Huber, W., and Anders, S. (2014). Moderated estimation of fold change and dispersion for RNA-seq data with DESeq2. Genome Biol. *15*, 550. https://doi.org/10.1186/s13059-014-0550-8.

99. Mi, H., Ebert, D., Muruganujan, A., Mills, C., Albou, L.P., Mushayamaha, T., and Thomas, P.D. (2021). PANTHER version 16: a revised family classification, tree-based classification tool, enhancer regions and extensive API. Nucleic Acids Res. *49*, D394–D403. https://doi.org/10.1093/nar/gkaa1106.

100. Mouse_Genome_Informatics. Mouse Genome Informatics, Human and Mouse Homology with Phenotype Annotations. http://www.informatics.jax.org/mgihome/nomen/index.shtml.

STAR★METHODS

KEY RESOURCES TABLE

REAGENT or RESOURCE	SOURCE	IDENTIFIER
Antibodies		
Anti-4C4	Gift from Hitchcock Lab	Raymond et al. (2006)[62]
Anti-Digoxigenin-AP, Fab fragments	MilliporeSigma	Cat# 11093274910; RRID: AB_2734716
Anti-pH3	MilliporeSigma	Cat# 06-570; RRID: AB_310177
Anti-phosphorylated-Erk	Cell Signaling	Cat# 4370; RRID: AB_2315112
Anti-total-Erk	Cell Signaling	Cat# 4696; RRID: AB_390780
Anti-acetylated tubulin	MilliporeSigma	Cat# T7451; RRID: AB_609894
Anti-tyrosine hydroxylase	MilliporeSigma	Cat# AB152; RRID: AB_390204
Chemicals, peptides, and recombinant proteins		
BCIP	Roche	Cat# 11383221001
BSA	Jackson ImmunoResearch	Cat# A9647-100G
NBT	Roche	Cat# 11383213001
NGS	Jackson ImmunoResearch	Cat# 005-000-121
Paraformaldehyde	Millipore sigma	Cat# P6148-500G
Neutral Red	Invitrogen	Cat# N3246
Trypsin EDTA, 0.5 M Solution, pH 8.0	Fisher Scientific	Cat# 15-400-054
Low Melt Agarose	American BioAnalytical	Cat# AB00981-000050
Deposited data		
RNA-sequencing data (*dyrk1a, scn1lab* mutants)	This paper	Deposited in Gene Expression Omnibus (GEO) at https://www.ncbi.nlm.nih.gov/geo/ Accession # GEO: GSE205578
Experimental models: Organisms/strains		
Zebrafish: 20 mutant lines	This paper (Table S1, Figure S1); Hoffman et al. (2016)[21]; Kroll et al. (2021)[77]	This paper; *cntnap2* mutants described in Hoffman et al. (2016)[21]; *scn1lab*$^{\Delta 44}$ mutants described in Kroll et al. (2021)[77]
Zebrafish: *scn1lab didy* mutant	Gift from de Witte Lab	Schoonheim et al. (2010)[28]
Oligonucleotides		
CRISPR gRNAs, TALENs, ZFNs	This paper (Table S1)	N/A
Primers for genotyping zebrafish mutant lines, *in situ* hybridization, and qPCR	This paper (Table S1)	N/A
Software and algorithms		
MATLAB	MathWorks	https://www.mathworks.com/products/trials.html/
BioImage Suite (Web App)	BioImage Suite Web	bioimagesuiteweb.org
BioImage Suite (Software Package)	BioImage Suite Web	https://github.com/bioimagesuiteweb/bisweb
Brain mapping code	This paper	https://github.com/ehoffmanlab/Weinschutz-Mendes-et-al-2023-mapping; Zenodo: https://doi.org/10.5281/zenodo.7644861
Imaris 9.9	Bitplane	https://imaris.oxinst.com
Graph Pad Prism	Dotmatics	https://www.graphpad.com
ImageJ	NIH	https://imagej.nih.gov/ij/download.html
ImageJ Cell Counter Plugin	N/A	https://imagej.nih.gov/ij/plugins/cell-counter.html
FSL maths	N/A	https://fsl.fmrib.ox.ac.uk/fsl/fslwiki/FslInstallation/MacOsX
Analysis of Functional NeuroImages (AFNI)	NIH	https://afni.nimh.nih.gov/pub/dist/doc/htmldoc/background_install/main_toc.html

(*Continued on next page*)

Continued

REAGENT or RESOURCE	SOURCE	IDENTIFIER
NodeJS	N/A	https://nodejs.org/en/
R and RStudio	CRAN	https://www.Rstudio.com
Sleep-wake behavioral analysis code	Prober et al. (2006)[29]; Rihel et al. (2010)[24]	https://github.com/JRihel/Sleep-Analysis/tree/Sleep-Analysis-Code; Zenodo: https://doi.org/10.5281/zenodo.7644073
Visual-startle analysis code	This paper	https://github.com/ehoffmanlab/Weinschutz-Mendes-et-al-2023-behavior; Zenodo: https://doi.org/10.5281/zenodo.7644898
Zebrafish to human developmental transcriptome code	Willsey et al. (2021)[13]	https://bitbucket.org/willseylab/

RESOURCE AVAILABILITY

Lead contact

Further information and requests for resources and reagents should be directed to and will be fulfilled by the Lead Contact, Ellen J. Hoffman (ellen.hoffman@yale.edu).

Materials availability

All zebrafish mutant lines generated in this study are available upon request with a completed Materials Transfer Agreement. A complete list of genotyping primers for these lines is provided (Table S1).

Data and code availability

- The raw and processed RNA sequencing data have been deposited at GEO and are publicly available as of the date of publication. Accession numbers are listed in the key resources table. Sleep-wake and visual-startle parameters (mean, SD, beta, p value) per genotype are shown in Table S2. All raw behavioral data from sleep-wake and visual-startle assays are available upon request. Regional quantification of brain volume (raw Jacobian determinants) for all mutants using the eight-region atlas is shown in Table S3. Regional quantification of brain activity (raw pERK/tERK values) for all mutants using the eight- and 149-region atlases is shown in Table S4. Raw confocal images are available upon request. Significant dysregulated pathways identified in homozygous and heterozygous *scn1lab*$^{\Delta 44}$ and *dyrk1aa*$^{\Delta 77}$*;dyrk1ab*$^{\Delta 8}$ mutants by PANTHER GO and GSEA using the Molecular Signatures Database are shown in Table S6.
- The code for comparing zebrafish and human developmental time course is described in Willsey et al. (2021).[13] The MATLAB code for sleep-wake analysis is described in Prober et al. (2006) and Rihel et al. (2010),[24,29] and is available on github at https://github.com/JRihel/Sleep-Analysis/tree/Sleep-Analysis-Code (Zenodo: https://doi.org/10.5281/zenodo.7644073). The MATLAB code for analyzing visual-startle responses is available on github at https://github.com/ehoffmanlab/Weinschutz-Mendes-et-al-2023-behavior (Zenodo: https://doi.org/10.5281/zenodo.7644898). Custom codes for whole-brain mapping are available on github at https://github.com/ehoffmanlab/Weinschutz-Mendes-et-al-2023-mapping (Zenodo: https://doi.org/10.5281/zenodo.7644861).
- Any additional information required to reanalyze the data reported in this paper is available from the lead contact upon request.

EXPERIMENTAL MODEL AND SUBJECT DETAILS

Animals

All procedures involving zebrafish were conducted in accordance with Institutional Animal Care and Use Committee (IACUC; Protocol #2021-20054) regulatory standards at Yale University. Zebrafish larvae were raised at 28°C on a 14:10 h light:dark cycle. Larvae were grown in 150 mm Petri dishes in blue water (0.3 g/L Instant Ocean, 1 mg/L methylene blue, pH 7.0) at a density of 60-80 larvae per dish. Assays were conducted in zebrafish embryos and larvae at 1-7 dpf. At these developmental stages, sex is not yet determined.

METHOD DETAILS

Generation of zebrafish mutant lines

To generate zebrafish ASD gene mutants, gene-specific CRISPR gRNAs (20 pg/CRISPR) and mRNA encoding Cas9 (200 pg) or sets of zinc finger nucleases (ZFN) (25-75 pg) or TALENs (50 pg) were injected into zebrafish embryos at the one-cell stage. See Table S1 for gRNA and ZFN/TALEN target sequences. The zebrafish paralogs of human ASD genes were identified by conducting a reciprocal

BLAST search of the zebrafish genome (Zv9). If two zebrafish paralogs were identified for a given gene, both were targeted simultaneously, generating double mutant fish. Percent amino acid identity compared to the human protein was determined using Clustal Omega.[78] CRISPRs were designed using ZiFit[79,80] and CRISPRscan, which was used to predict off-target sites.[81] ZFN were designed by Sigma-Aldrich and TALENs were designed by the University of Utah HSC Cores Research Facility.[82] Germline mutations in founders were confirmed by Sanger sequencing (Table S1, Figure S1). Founders (F0) were crossed to wild-type fish to generate double heterozygotes, which were incrossed to generate double homozygous mutants. Mutant lines were outcrossed to wild-type fish for at least one generation and genotyping was used to confirm the presence of mutations in each generation. Genotyping primers and procedures for all mutant lines are shown in Table S1. The *scn1lab*^{didy} mutant line[28] was obtained from the laboratory of Dr. Peter de Witte.

Whole mount *in situ* hybridization

PCR primers used to generate *in situ* probes are shown in Table S1. Probes were amplified from cDNA samples from zebrafish embryos (0-48 hpf) and larvae (72-120 hpf) and cloned into pBluescript, pCRII-TOPO, or pCR-Blunt II-TOPO. Antisense digoxigenin (DIG)-labeled RNA probe synthesis was performed according to the following method.[21] Probes were synthesized for 3 h at 37°C in 20 μL reactions containing: 2 μL 10X transcription buffer (Roche), 2 μL 10X DIG RNA labeling mix (Roche), 1 μL 100 mM DTT (Roche), 1 μL RNaseOUT recombinant ribonuclease inhibitor (Invitrogen), 2 μL RNA polymerase (T7, SP6, or T3) (Roche), and 12 μL of linearized purified plasmid. Following probe synthesis, 2 μL of DNase I (amplification grade) (Invitrogen) was added to each sample for 30 min at 37°C. Probes were purified using the RNeasy Mini Kit (Qiagen).

Whole mount *in situ* hybridization was performed according to the method of Thisse et al. (1993).[83] Specifically, 24-48 hpf embryos were raised in 0.003% 1-phenyl-2-thiourea (PTU) in blue water (0.3 g/L Instant Ocean, 1 mg/L methylene blue, pH 7.0) to prevent pigment formation and fixed in 4% paraformaldehyde (PFA) overnight at 4°C. Embryos were then washed in PBSTw (PBS +0.1% Tween 20), dehydrated sequentially in methanol/PBSTw, and stored at −20°C in 100% methanol at least overnight. Embryos were sequentially rehydrated, washed in PBSTw, and digested with proteinase K at a final concentration of 10 μg/mL for 11-12 min (24 hpf) or 40 min (48 hpf). After washing in PBSTw, samples were refixed in 4% PFA for 20 min at room temperature and washed in PBSTw. Next, samples were incubated in pre-warmed hybridization buffer (50% formamide, 4X SSC buffer, 0.1% Tween 20, 9.2 mM citric acid, 50 μg/mL Heparin, 500 μg/mL tRNA) for 3 h at 65°C, then incubated overnight at 65°C in hybridization buffer containing 100-200 ng of each RNA probe. Samples were then transferred sequentially from hybridization buffer to 2X SSC buffer (3.0 M sodium chloride and 0.3 M sodium citrate) at 65°C, incubated in 2X SSC buffer for 15 min and 0.2X SSC buffer for 1 h (2 × 30 min) at 65°C. Samples were transferred sequentially from 0.2X SSC buffer to PBSTw at room temperature, incubated in blocking solution (15% normal sheep serum, 2 mg/mL BSA in PBSTw) for 2 h at room temperature, and then in antibody solution (anti-Digoxigenin-AP, Fab fragments, Millipore Sigma, Cat# 11093274910) diluted 1:5000 in 2% normal sheep serum and 2 mg/mL BSA in PBSTw) overnight at 4°C. Samples were washed in PBSTw and incubated in staining buffer (100 mM tris HCl, pH 9.5, 50 mM $MgCl_2$, 100 mM NaCl, 0.1% Tween 20) for a total of 15 min (3 × 5 min) at room temperature. Samples were transferred to staining solution (100 mg/mL NBT (Roche) and 50 mg/mL BCIP (Roche) in staining buffer), and incubated at room temperature in the dark until staining became visible. The reaction was stopped by removing the staining solution and washing in 4% PFA. Stained embryos were incubated overnight in 4% PFA, washed in PBSTw, and later cleared in 100% glycerol for imaging at 40x or 85x using a dissecting stereomicroscope.

Zebrafish time course transcriptomic analysis

RNA sequencing raw count data from wild-type zebrafish at 16 hpf to 5 dpf (whole-body) in the HLF background[30] and wild-type 6 dpf zebrafish brains in the *scn1lab*$^{\Delta 44}$ genetic background (see "RNA extraction and sequencing") were used. To compare the zebrafish developmental time course to human brain development, we utilized methods and code developed by the laboratory of Jeremy Willsey. Using raw count data, zebrafish genes were first mapped to human genes using Ensembl BioMart (version GRCz10/danRer10)[84] according to the gene mapping method described below (see "RNA-Seq pathway analysis"). Next, we performed a principal component analysis (PCA) of the BrainSpan human brain developmental transcriptome dataset[31] and projected the zebrafish datasets to PCA coordinate space, as in Willsey et al. (2021).[13] We used the BrainSpan RNA-seq (Gencode v10) dataset summarized to gene level. This dataset was subset to expressed genes defined as those having greater than three RPKM in at least five samples, as in Willsey et al. (2021).[13] Briefly, all gene expression datasets were reduced to a common gene set between the zebrafish and human datasets (2,192 genes). In the zebrafish dataset, human gene orthologs in zebrafish that had multiple transcripts were collapsed and the median value across the five replicates (whole-body) or three replicates (brain-only) was retained. We transformed the zebrafish and BrainSpan RNA-seq datasets into $\log_2$(RPKM). To visualize developmental trajectories, the BrainSpan and zebrafish datasets were zero centered and scaled before calculating and projecting onto the principal components. An equivalent vector representing the scaled and centered zebrafish time course data was projected onto the BrainSpan PCA coordinate space using center point and rotations, as in Willsey et al. (2021).[13]

qPCR

qPCR primer sequences for each gene are shown in Table S1. qPCR primer sequences for *katnal2* were obtained from Zheng et al. (2022).[85] Total RNA was isolated from zebrafish larvae or juvenile fish using the RNeasy Plus Micro Kit (Qiagen). cDNA was

synthesized using the SuperScript III First-Strand Synthesis System (Invitrogen). qPCR was performed using a CFX96 machine (Bio-Rad) and Power SYBR Green PCR Master Mix (Applied Biosystems). Two to four replicate experiments were performed per gene. The following mutant lines and wild-type fish at matched developmental stages were used: *cul3a*$^{\Delta 7/\Delta 7}$*cul3b*$^{\Delta 32/\Delta 20}$ and *scn1lab*$^{\Delta 44/\Delta 5}$ (5 dpf); *tbr1a*$^{\Delta 64/\Delta 19}$*tbr1b*$^{\Delta 10/\Delta 14}$ (7 dpf); *chd8*$^{\Delta 5/\Delta 7}$, *dyrk1aa*$^{\Delta 77/4ins}$*dyrk1ab*$^{\Delta 8/\Delta 5}$, *grin2ba*$^{\Delta 25/\Delta 4}$*grin2bb*$^{\Delta 64/\Delta 4}$, *katnal2*$^{\Delta 19/\Delta 4}$, *kdm5ba*$^{\Delta 17/4ins}$*kdm5bb*$^{\Delta 14/\Delta 4}$; *pogza*$^{\Delta 23/\Delta 5}$*pogzb*$^{\Delta 22/\Delta 20}$ (*pogzb*) (14-18 dpf); *pogza*$^{\Delta 23/\Delta 5}$*pogzb*$^{\Delta 22/\Delta 20}$ (*pogza*) (24 hpf). 24 hpf was used for *pogza* because it has been shown to be expressed up to 48 hpf and its expression at juvenile stages has not been shown.[86] Statistical analyses were conducted and boxplots were generated using GraphPad Prism (Dotmatics).

Brain volume and activity mapping

Whole-mount immunostaining with antibodies to total-ERK and phosphorylated-ERK for brain volume and activity mapping was performed following the method of ref. [22] and [42] with some modifications. Specifically, zebrafish larvae at 6 dpf were collected by pouring larvae into a mesh sieve and immediately immersing the sieve into 4% PFA/4% sucrose in PBS +0.25% Triton (PBST). Larvae were fixed overnight at 4°C and washed in PBST. To control for background variation, larvae from all mutant lines were generated from heterozygous incrosses with fixation performed blind to genotype. Genotyping was performed the day after fixation by tail clipping followed by DNA extraction. PCR was performed using fluorescent-labeled (fluorescein (5′ 6-FAM) or hexachlorofluorescein (5′ HEX)) PCR primers, using high-resolution fragment analysis (DNA Analysis Facility at Yale University; Yale Keck DNA Sequencing Facility). To improve antibody penetration, brains were dissected prior to immunostaining, as in Wilson et al. 1990.[87] Briefly, larvae were pinned on the side in a sylgard dish using two dissecting pins. Using a tungsten needle and forceps, the eyes and the skin tissue on the surface of the brain were removed. The jaw, cardiac tissue, and yolk were also removed. Dissected brains were incubated in 150 mM Tris-HCl for 15 min at 70°C, washed in PBST, permeabilized in 0.05% Trypsin-EDTA for 45 min on ice, and washed in PBST. To remove any residual skin pigment, depigmentation was performed by incubating samples in 1.5% H_2O_2 and 50 mM KOH for 15 min. Brains were blocked for 1 h in PBST with 1% BSA, 2% normal goat serum (NGS) and 1% DMSO, and incubated overnight at 4°C in primary antibodies to pERK (Cell Signaling #4370) and tERK (Cell Signaling #4696) diluted at 1:500 in blocking solution without NGS. After overnight incubation, samples were washed in PBST and incubated for 2 h at room temperature with Alexa-fluorophore-conjugated secondary antibodies (Life Technologies) at a dilution of 1:200 in blocking solution without NGS. Dissected brains were mounted dorsally in low melting point agarose (1-2%) and imaged by confocal microscopy at 25X (0.95W) using z-stacks ranging from ~200 to 300 μm (Leica Systems, Yale Center for Cellular and Molecular Imaging). Experiments were performed in two to four independent clutches for each ASD gene. Total sample sizes are shown in Table S7.

Behavioral assays

Behavioral assays were performed by placing individual larvae in a 96-well plate (7701-1651; Whatman, Clifton, NJ) containing 650 μL of standard embryo water per well (0.3 g/L Instant Ocean, 1 mg/L methylene blue, pH 7.0) within a Zebrabox (Viewpoint Life Sciences, Montreal, QC, Canada). Larval movement was recorded with a monochrome camera using ZebraLab quantization mode and quantified using an automated video tracking system (Zebrabox and ZebraLab software). The ZebraLab detection parameters were empirically defined for detection of larval movement with minimal noise. The visual-startle assay was adapted from Scott et al. (2016)[34] with some modifications and conducted in larvae at 5 dpf. ZebraLab quantization mode (Zebrabox and ZebraLab software) was used to record larval activity every 1 s. To test larval responses to lights-off stimuli, larvae were acclimated to white light background illumination for 1 h, after which their baseline activity was tracked for 30 min followed by five 1-s flashes of darkness at 29-s intervals (Figure 2B). To test responses to lights-on stimuli, the assay was then reversed, where larvae were acclimated to darkness and then exposed to 1-s flashes of bright white light at 29-s intervals. Using custom MATLAB software developed by our lab (available on github at https://github.com/ehoffmanlab/Weinschutz-Mendes-et-al-2023-behavior; https://doi.org/10.5281/zenodo.7644898), the following six behavioral parameters were quantified for both lights-off and lights-on stimuli (Figure 2B): (i) average intensity of all startle responses (AVG STIM); (ii) average post-stimulus activity (AVG POST); (iii) average activity after the first stimulus (POST1); (iv) stimulus versus post-stimulus activity (STIMvPOST); (v) and (vi) intensity of responses to the first (S1) and last (S5) stimuli, reflecting habituation, respectively.

The sleep-wake assay[24,29] was conducted in larvae at 5-7 dpf after the visual-startle assays. Specifically, larvae were exposed to a 14h:10h white light:dark schedule with constant infrared illumination within a Zebrabox (Viewpoint Life Sciences). Using custom MATLAB software developed by Jason Rihel (available on github at (https://github.com/JRihel/Sleep-Analysis/tree/Sleep-Analysis-Code; https://doi.org/10.5281/zenodo.7644073)), the following six behavioral parameters were quantified during the day and night at 6-7 dpf (Figure 2B): (i) total activity; (ii) total sleep; (iii) waking activity; (iv) rest bouts; (v) sleep length; (v) sleep latency.[24]

To control for genetic background, behavior assays were performed blind to genotype using sibling- or cousin-matched larvae from heterozygous incrosses of all mutant lines (Table S1). Genotyping was performed after each experiment. Experiments were performed at least in triplicate for each line to obtain sample sizes of ~40-50 homozygous and wild-type fish. Total samples sizes of homozygous, heterozygous, and wild-type fish for all behavioral experiments are shown in Table S7.

RNA extraction and sequencing

Total RNA was extracted from isolated larval heads with the eyes removed (n = 3-4 heads per genotype, 1 head per sample). To control for genetic background, RNA was extracted from sibling- or cousin-matched larvae from heterozygous incrosses of *scn1lab*$^{\Delta 44/+}$

and *dyrk1aa*$^{\Delta 77/+}$*dyrk1ab*$^{\Delta 8/+}$ fish. DNA was isolated from 3 dpf larvae using the Zebrafish Embryonic Genotyper (ZEG) system (wFluidx, Salt Lake City, UT, USA) and genotyping was performed using high-resolution fragment analysis (DNA Analysis Facility at Yale University; Yale Keck DNA Sequencing Facility). Larvae were separated by genotype at 4 dpf and raised in a 6-well plate at 28°C in blue water (0.3 g/L Instant Ocean, 1 mg/L methylene blue, pH 7.0). At 6 dpf, larvae were euthanized on ice for 15 min, after which the heads were isolated, and the eyes were removed using a fine scalpel. RNA was immediately extracted using the RNeasy Micro Kit (Qiagen). RNA library preparation was performed using NEBNext Single Cell Low Input RNA Library Prep Kit (Cat# E6420L) and sequenced at 25 million reads/sample using NovaSeq 6000 (Illumina) (Yale Center for Genome Analysis). Raw reads from all RNA-seq experiments have been deposited at Gene Expression Omnibus (GEO) (Accession # GEO: GSE205578) (https://www.ncbi.nlm.nih.gov/geo/).

dyrk1a body length measurements

Homozygous *dyrk1aa*$^{\Delta 77/\Delta 77}$*dyrk1ab*$^{\Delta 8/\Delta 8}$ and unrelated wild-type larvae were imaged live at 6 dpf using a dissecting stereomicroscope. A single blinded rater measured body length using Fiji.[88] Statistical analyses were conducted and boxplots were generated using GraphPad Prism (Dotmatics).

Immunohistochemistry

Whole mount antibody staining of dissected embryos was performed as described in Wilson et al. (1990)[87] with some modifications. Specifically, larvae were fixed in 4% sucrose/4% PFA at room temperature for 1 h per 24 h of development. Following fixation, larvae were washed in PBS and brains were dissected as described above (see "Brain volume and activity mapping")[87] then dehydrated sequentially in methanol-PBST (PBS +0.5% Triton X-100) and stored in methanol at −20 °C at least overnight. Brains were rehydrated sequentially, washed in PBST, and permeabilized with either proteinase K at 20-40 μg/mL for 20 min (4C4, tyrosine hydroxylase, acetylated tubulin) or 0.05% Trypsin-EDTA for 30 min followed by 100% acetone on ice for 7 min (pH3, acetylated tubulin). After permeabilization, brains were post-fixed in 4% PFA for 20 min at room temperature (4C4, tyrosine hydroxylase staining). Brains were blocked for at least 1 h at room temperature in 10% NGS, 1% DMSO and 10% BSA in PBST, and incubated in primary antibodies at a dilution of 1:500 in block solution without NGS overnight at 4°C. Samples were washed 4-6 times for at least 30 min in PBST and incubated for 2 h at room temperature with Alexa-fluorophore-conjugated secondary antibodies (Life Technologies) at a dilution of 1:200 in blocking solution without NGS. After washing with PBST, zebrafish larvae were mounted in low melting point agarose (1-2%) for imaging. The following primary antibodies were used: anti-4C4 (generous gift from the lab of Dr. Peter Hitchcock), anti-pH3 (Millipore Sigma #06-570), anti-tyrosine hydroxylase (Millipore Sigma #AB152), and anti-acetylated tubulin (Millipore Sigma #T7451). Background-matched wild-type, heterozygous, and homozygous larvae from *scn1lab*$^{\Delta 44/+}$ incrosses were used. Homozygous *dyrk1aa*$^{\Delta 77/\Delta 77}$*dyrk1ab*$^{\Delta 8/\Delta 8}$ fish were compared to unrelated wild-type fish. Statistical analyses were conducted and boxplots were generated using GraphPad Prism (Dotmatics).

Confocal imaging and cell quantification

Whole-mount immunostained embryos were imaged by confocal microscopy (Leica Systems, Yale Center for Cellular and Molecular Imaging). Maximum intensity projections are shown for all confocal images, which were processed using Fiji.[88] Image brightness and contrast were adjusted equally for all genotypes using Fiji.[88] Figures were assembled using Illustrator (CC, Adobe). Imaris 9.9 (Bitplane) was used to quantify the number of pH3+ and 4C4+ cells. All images were analyzed blind to genotype by a single rater. For quantifying pH3+ cells using Imaris, surfaces were drawn using landmarks to identify the forebrain and midbrain-hindbrain boundaries. The green channel (pH3) was masked for each region using the rendered surface. Spots were then applied to the region-specific masked channels using background subtraction and estimated XY diameter = 5.0 μm, and filtered by quality with cutoff 3.80 to identify pH3+ cells in the forebrain, midbrain, and whole brain. Each spot counted as one pH3+ cell. Quantification of 4C4+ cells was performed using the Imaris 9.9 LabKit pixel classification method plugin through ImageJ. Imaris Surfaces were created and trained using machine learning pixel classification from LabKit to specifically identify 4C4+ cells within the masked green channel for the whole brain and forebrain. The trained algorithm was applied to each image followed by seed point (12.0 μm) generation to split cells based on morphology. The surface was rendered and filtered by quality with a cutoff of 1.75 (*dyrk1a*) and −3.75 or −4.0 (*scn1lab*, replicate experiments). All surfaces passing this threshold of any voxel size were selected. Each surface was counted as one microglial cell. To quantify TH+ cells, the forebrain and posterior tuberculum were identified according to Nunes et al. (2021) and Sallinen et al. (2009)[89,90] and quantified using the ImageJ Cell Counter plug-in. Statistical analyses were conducted and boxplots were generated using GraphPad Prism (Dotmatics).

Neutral red staining

For phenotypic analyses of microglia in live fish, a surface neutral red stain was used.[61] Background-matched siblings from *scn1lab*$^{\Delta 44/+}$ heterozygous incrosses and homozygous *dyrk1aa*$^{\Delta 77/\Delta 77}$*dyrk1ab*$^{\Delta 8/\Delta 8}$ and unrelated wild-type zebrafish larvae at 4 dpf were used. Fish were collected and treated daily with 0.003% 1-phenyl-2-thiourea (PTU) diluted in methylene blue embryo water to inhibit pigmentation. At 4 dpf, larvae were incubated in embryo water containing 2.5 μg/mL neutral red at 28°C for 4–5 h, and embryo water was replaced three times prior to imaging. Live images were acquired using an upright dissecting

stereomicroscope. Quantification of neutral red+ cells was performed blind to genotype by a single rater using the ImageJ Cell Counter plug-in. Statistical analyses were conducted and boxplots were generated using GraphPad Prism (Dotmatics).

QUANTIFICATION AND STATISTICAL ANALYSIS

Imaging registration for brain volume and activity analysis

Confocal z stack images of tERK and pERK-stained brains were used to quantify regional differences in brain volume and activity as in Randlett et al. (2015),[42] using custom MATLAB software developed by our lab, which is available on github at https://github.com/ehoffmanlab/Weinschutz-Mendes-et-al-2023-mapping (https://doi.org/10.5281/zenodo.7644861). Specifically, our image registration and analysis pipeline utilized BioImage Suite Web Tools[91] and included the following steps (Figures 3A and 4A).

Pre-processing

1. Confocal z stack images of tERK-immunostained brains were nonlinearly registered to a standard reference brain[42] using transformation-based deformation.[92,93] This generates a transformation file that describes the degree of stretch or compression required for mapping to the reference image. Brain size and activity differences were visualized using BioImage Suite Web.[91]

Volume quantification

2. The determinant of the Jacobian of the deformation field was used to quantify local volume differences between the registered images and a 2 × 2 × 2 resampled version of the standard reference zebrafish brain. (i.e. 1 = no volume change, >1 = individual subject is larger than the template and <1 = individual subject is smaller than the template) (Staib et al., 2006),[92] as was done in our previous work in humans.[93]
3. Regional differences in brain volume were calculated using the 8-region zebrafish brain atlas, which was derived manually from a resampled standard zebrafish brain (Z-brain) atlas.[22,42]
4. Linear mixed modeling was applied to raw Jacobian values to identify significant differences in brain volume across experiments (see "Brain volume and activity analysis" below).
5. The boxplot shown in Figure 3E shows the regional differences in brain volume relative to the standard zebrafish reference brain.[42] Statistical analyses were conducted in StatPlus (AnalystSoft) and boxplots were generated in GraphPad Prism (Dotmatics).

Activity quantification

6. For brain activity calculations, the geometric transformation is applied to the pERK confocal z stack images.
7. pERK image intensities were normalized by tERK intensities through a voxel-wise division (pERK/tERK).
8. The average pERK/tERK intensities were calculated within individual regions delineated in the Z-brain atlas.[42] The 8-region and 149-region atlases were derived manually from versions of the Z-brain atlas.[22,42] To generate the 149-region atlas (Figure 5A), 65 regions were excluded from the original Z-brain atlas because these regions were either removed in dissected brains (e.g. eyes, trigeminal ganglion) or located in the posterior hindbrain (e.g. regions caudal to rhombomere 4), which was not imaged. The 149-region atlas consists of four major subdivisions: *(i)* telencephalon, including the pallium and subpallium (17 regions); *(ii)* diencephalon, including the thalamus, hypothalamus, and posterior tuberculum (71 regions); *(iii)* mesencephalon, including the optic tectum and tegmentum (11 regions); *(iv)* rhombencephalon (46 regions); and *(v)* 4 regions that are not considered part of these major regions (Figure S5A).
9. Linear mixed modeling was applied to raw pERK/tERK values to identify significant differences in brain activity across experiments (see "Brain volume and activity analysis" below).
10. The boxplot in Figure 4D shows regional differences in brain activity (normalized pERK/tERK ratios). Statistical analyses were conducted in StatPlus (AnalystSoft) and boxplots were generated in GraphPad Prism (Dotmatics).

Visualization of brain volume and activity phenotypes

BioImage Suite Web (2022)[91] was used to visualize differences in brain volume and activity in homozygous and heterozygous mutants versus wild-type background-matched fish. Images for volume and activity were overlayed on a resampled standard reference fish. We calculated a voxel-wise Z-scored value of homozygous and heterozygous images compared to background-matched wild-type fish using the mean and standard deviation of Jacobian determinant (volume) or pERK/tERK (activity) values. Hypothesis testing for activity was performed at the voxel level using AFNI 3dttest comparing homozygous and heterozygous fish to background-matched wild-type fish, generating an index of voxel coordinates deemed significantly different between genotypes. We visualized volume differences by mapping *Z* score values from 3.3-6 (Figure 3F) or 2.4–5.2 (Figures 3G and S3B). To visualize activity images, we used FWE correction on this index determined by Monte Carlo simulation using the AFNI 3dClustSim version (16.3.05, October 2016) program.[94] Visualizations for activity are shown at $p < 0.05$ whole-brain FWE corrected with an initial *P* threshold of <0.0001 for *scn1lab*$^{\Delta44/\Delta44}$ and <0.05 for the following mutant lines: *chd8*$^{\Delta5/\Delta5}$, *dyrk1aa*$^{\Delta77/\Delta77}$*dyrk1ab*$^{\Delta8/\Delta8}$, *kdm5ba*$^{\Delta17/\Delta17}$*kdm5bb*$^{\Delta14/\Delta14}$, *cntnap2a*$^{\Delta121/\Delta121}$*cntnap2b*$^{31ins/31ins}$. *tbr1a*$^{\Delta64/\Delta64}$*tbr1b*$^{\Delta10/\Delta10}$ was not FWE corrected because

significance for this mutant did not meet cluster correction. For activity and volume, images were generated using mosaic and orthogonal views in BioImage Suite Web to capture cross sectional increases and decreases in the axial and sagittal planes. All axial mosaics are shown starting at Z level of 90 and decreasing by 7 slices for each image. Sagittal mosaics are displayed starting at X level of 169 and decreasing by 7 slices for each image.

Brain volume and activity analysis

Linear mixed models (LMM) were used to compare volume and activity in each brain region in homozygous, heterozygous, and background-matched wild-type fish for each genotype. The variations of brain volume and activity across experiments were accounted for by including the date of the experiment as a random effect in LMM. Hierarchical clustering analysis was performed to cluster mutants and brain regions based on the signed -$\log_{10}$-transformed p values from LMM, where sign is the direction of the difference in volume or activity when comparing between the mutant and wild-type. Clustergram ("pheatmap: Pretty heatmaps" (RRID:SCR_016418): https://cran.r-project.org/web/packages/pheatmap/index.html) was used to visualize mutant clusters and brain region clusters in a heatmap.

To compare volume and activity in each brain region across all genotypes (Figures 3H, 4G, S3E, S3F, S4G and S4H), we assessed the overall difference by combining the genotype-level p values using Fisher's method. Bonferroni adjustment was used to correct for multiple comparisons. Brain regions with adjusted p value <0.05 were considered to be significant. To determine the regions with the largest volume change, we pooled β values from LMM for each region across all homozygous mutants using inverse-variance weighting.[95]

Behavioral analysis

LMM were used to compare phenotypes of each behavioral parameter between homozygous and heterozygous mutant versus wild-type fish for each genotype. The variations of behavioral phenotype across experiments were accounted for by including the date of the experiment as a random effect in LMM. We analyzed 24 behavioral parameters from the visual-startle lights-on and lights-off assays and the sleep-wake assay. Hierarchical clustering analysis was performed to cluster mutants and behavioral parameters based on the signed -$\log_{10}$-transformed p values from LMM, where sign is the direction of the difference in behavioral phenotype when comparing between the mutant and wild-type. Clustergram ("pheatmap: Pretty heatmaps" (RRID:SCR_016418): https://cran.r-project.org/web/packages/pheatmap/index.html) was used to visualize mutant clusters and behavioral parameter clusters in a heatmap.

Pearson correlation analysis was performed to evaluate correlations between mutants based on the difference in the 24 behavioral parameters, where the difference was assessed using the signed -$\log_{10}$-transformed p values. Hierarchical clustering analysis was performed to cluster mutants based on pairwise correlations. Correlograms were used to visualize mutant clusters and their correlations.

Identification of differentially expressed genes from RNA-seq data

To identify DE genes, low quality reads were trimmed and adaptor contamination was removed using Trim Galore (v0.5.0, https://www.bioinformatics.babraham.ac.uk/projects/trim_galore/). Trimmed reads were mapped to the *Danio rerio* reference genome (GRCz11) using HISAT2 (v2.1.0).[96] Gene expression levels were quantified using StringTie (v1.3.3b)[97] with gene models (release 103) from Ensembl. Differential expression analysis was conducted using DESeq2 (v 1.22.1).[98] DEseq2 results have been deposited at Gene Expression Omnibus (GEO) (https://www.ncbi.nlm.nih.gov/geo/info/seq.html). (Accession # GEO: GSE205578)

RNA-seq pathway analysis

To understand the biological functions of DE genes, we performed functional pathway analysis using Gene Set Enrichment Analysis (GSEA)[49,50] and PANTHER.[99] We first mapped zebrafish genes to human orthologs using Ensembl BioMart (version GRCz10/danRer10).[84] For duplicated genes, we used the following gene mapping assignments: (i) if multiple human genes mapped to the same zebrafish gene, then each human gene was assigned to the zebrafish gene; (ii) if multiple zebrafish genes map to the same human gene, then the zebrafish gene with the highest average expression among samples was assigned to the human gene. In the GSEA analysis, enrichment scores were calculated for all mapped genes. A nominal p value for the maximal enrichment score was obtained based on 1,000 random permutations. Significance was adjusted using false discovery rate (FDR) to account for multiple hypothesis testing. Pathways with FDR Q value < 0.25 were considered to be significant as recommended by the GSEA software. For PANTHER, DE genes with p value <0.05 were included in the analysis. Fisher's exact test was used to determine the representation of a specific functional pathway among the selected DE genes. Pathways with FDR <0.05 were considered to be significant.

Gene set and cell type enrichment analysis

To test whether human gene sets of interest are over-represented in the DE genes of each mutant, we first mapped zebrafish DE genes with p value <0.1 and fold-change >1.5 to human orthologs using Ensembl BioMart (version GRCz10/danRer10)[84] and then performed Fisher's exact test to assess the enrichment in the upregulated and downregulated genes separately. p-value <0.05 was considered to be significant. To identify the top co-expression networks[9] that are the most significant in both mutants (Figure 6G), we calculated the combined p value in homozygous mutants using Fisher's method.

Mouse brain cell type markers were obtained from Cahoy et al. 2008, Poulin et al. 2014, and Zeisel et al. 2015.[58–60] To test whether the cell type markers are over-represented in the DE genes of each mutant, we first mapped zebrafish DE genes with p value <0.1 and fold-change >1.5 to human orthologs using Ensembl BioMart (version GRCz10/danRer10)[84] and obtained genome-wide one-to-one human-mouse orthologs from the Mouse Genome Informatics (MGI) resource.[100] Fisher's exact tests were performed to assess the enrichment in the upregulated and downregulated genes separately. p-value <0.05 was considered to be significant.